

Optical profiling of autonomous Ca^{2+} nanodomains generated by lysosomal TPC2 and TRPML1

Lianne C. Davis[#], Anthony J. Morgan[#], Antony Galione^{*}

Department of Pharmacology, University of Oxford, Mansfield Road, Oxford, OX1 3QT, UK

ARTICLE INFO

Keywords:

TPC2
TRPML1
Lysosome
 Ca^{2+}
Phagocytosis
Macrophages

ABSTRACT

Multiple families of Ca^{2+} -permeable channels co-exist on lysosomal Ca^{2+} stores but how each family couples to its own unique downstream physiology is unclear. We have therefore investigated the Ca^{2+} -signalling architecture underpinning different channels on the same vesicle that drive separate pathways, using phagocytosis as a physiological stimulus. Lysosomal Ca^{2+} -channels are a major Ca^{2+} source driving particle uptake in macrophages, but different channels drive different aspects of Fc-receptor-mediated phagocytosis: TPC2 couples to dynamin activation, whilst TRPML1 couples to lysosomal exocytosis. We hypothesised that they are driven by discrete local plumes of Ca^{2+} around open channels (Ca^{2+} nanodomains). To test this, we optimized Ca^{2+} -nanodomain recordings by screening panels of genetically encoded Ca^{2+} indicators (GECIs) fused to TPC2 to monitor the $[\text{Ca}^{2+}]$ next to the channel. Signal calibration accounting for the distance of the GECI from the channel mouth reveals that, during phagocytosis, TPC2 generates local Ca^{2+} nanodomains around itself of up to 42 μM , nearly a hundred-fold greater than the global cytosolic $[\text{Ca}^{2+}]$ rise. We further show that TPC2 and TRPML1, though on the same lysosomes, generate autonomous Ca^{2+} nanodomains of high $[\text{Ca}^{2+}]$ that are largely insulated from one another, a platform allowing their discrete Ca^{2+} -decoding to promote unique respective physiologies.

1. Introduction

Upon cell stimulation by extracellular cues, an ubiquitous signal transduction modality is an increase in the intracellular $[\text{Ca}^{2+}]$ upon opening of Ca^{2+} -permeable channels in the plasma membrane (Ca^{2+} influx) or in the membranes of Ca^{2+} -storing organelles (Ca^{2+} release) [1]. Although $[\text{Ca}^{2+}]$ will increase globally in the cytosol up to hundreds of nanomolar, it is now evident that Ca^{2+} increases heterogeneously in local 'hot-spots' around the Ca^{2+} channels themselves owing to restricted Ca^{2+} diffusion [2]. This architecture underpins Ca^{2+} -signal compartmentation whereby Ca^{2+} is delivered selectively where (and when) it is required in sub-regions of the cell corresponding to uniquely positioned Ca^{2+} -decoding proteins (and/or organelles) [2]. These private conversations between Ca^{2+} -channels and their cognate Ca^{2+} -binding proteins mean that extracellular stimuli couple to a unique and isolated downstream physiological cascade by judicious selection of the appropriate Ca^{2+} channel.

To the canonical organellar Ca^{2+} channels of the ER (IP_3 receptors, IP_3Rs , and ryanodine receptors, RyRs) have been added families of Ca^{2+} -

permeable channels on acidic Ca^{2+} stores (that include endosomes and lysosomes) [3,4]. Amongst the latter channel families are the mucolipins (TRPMLs) and two-pore channels (TPCs) which exist as multiple isoforms, each of which is selectively targeted to its particular endo-lysosomal vesicle class in an isoform-specific manner, with lysosomes enriched in TRPML1 and TPC2 [3]. Mechanistically, both TRPML1 and TPC2 can be activated by the lysosome-specific membrane-lipid, $\text{PI}(3,5)\text{P}_2$, but TPC2 can be additionally gated by the cytosolic second messenger, NAADP [5,6]. Importantly, these two channel families are non-redundant and are implicated in mutually exclusive downstream physiological processes including TFEB activation [7], lysosomal volume [8], choroidal angiogenesis [9], macropinosome resorption [10] and oxytocin neurosecretion [11]. How these channels segregate their respective signalling circuitry is currently undefined.

The total amount of Ca^{2+} that can be released from lysosomes is small compared with the ER and, consequently, pure lysosomal Ca^{2+} signals are often barely detectable in global recordings of cytoplasmic Ca^{2+} [12] (although transient, highly localized cytoplasmic Ca^{2+} events are sometimes detectable [13,14]). Their small size means that

^{*} Corresponding author.

E-mail address: antony.galione@pharm.ox.ac.uk (A. Galione).

[#] These authors contributed equally.

<https://doi.org/10.1016/j.ceca.2023.102801>

Received 4 August 2023; Received in revised form 30 August 2023; Accepted 17 September 2023

Available online 18 September 2023

0143-4160/© 2023 The Authors. Published by Elsevier Ltd. This is an open access article under the CC BY license (<http://creativecommons.org/licenses/by/4.0/>).

lysosomes are better suited to signalling via locally high Ca^{2+} domains immediately around lysosomal Ca^{2+} channels [12] which are not readily sensed by bulk cytoplasmic Ca^{2+} reporters. These domains might drive specific major physiological processes that other, distal Ca^{2+} sources cannot, and lysosomes are involved in the pathogenesis of an increasing number of diseases, including dementia, infection and cancer [15–17]. The magnitude and spatial spread of these local Ca^{2+} signals are, however, unknown.

To gain traction into this unsolved issue, we have exploited phagocytosis as a convenient model physiological system. The uptake of opsonized particles by macrophages is Ca^{2+} -dependent, but the source (s) of Ca^{2+} has long been controversial [18]. Recently, we showed that endo-lysosomal Ca^{2+} stores, which have previously been overlooked, were in fact major Ca^{2+} sources that underpin Fc-receptor-mediated phagocytosis, whereas the ER and Ca^{2+} influx were quite dispensable [19]. More remarkably, different channels (TPC2 and TRPML1) on the same lysosomal Ca^{2+} stores were not only differentially recruited by different-sized particles, but also coupled to different downstream pathways (i.e. dynamin activation and lysosomal exocytosis respectively) [19,20].

However, the signalling architecture underlying such extreme Ca^{2+} compartmentation has not been explicitly defined and it is unclear what is so unique about these lysosomal Ca^{2+} signals. Is the amplitude of lysosomal Ca^{2+} nanodomains sufficiently large to drive phagocytosis? Are Ca^{2+} nanodomains generated by TPC2 and TRPML1 channels spatially segregated from one another to permit the recruitment of autonomous signalling pathways? These issues are not peculiar to phagocytosing macrophages but are ill-defined across all cell types, even though these channel families are ubiquitous, and therefore answering these questions is of universal importance.

Hitherto, lysosomal Ca^{2+} nanodomains have not been characterized in terms of their absolute $[\text{Ca}^{2+}]$ or spatial spread, due in part to the technical challenges of measuring such highly localized responses compounded by the potential Ca^{2+} spill-over from other Ca^{2+} sources. Exploiting the physiological platform of macrophage phagocytosis as a window into lysosomal channel signalling compartmentation, we have screened panels of different GECIs (genetically encoded Ca^{2+} indicators) fused to channels in order to define the optimal GECI properties for selectively monitoring local lysosomal $[\text{Ca}^{2+}]$. Thereby, we have quantified the TPC2 Ca^{2+} nanodomain as being up to 2-orders of magnitude greater than the global cytosolic signal. Furthermore, the Ca^{2+} nanodomains of activated TPC2 and TRPML1 channels were largely insulated from one another, providing a framework for their independent Ca^{2+} signalling without cross-contamination of cellular circuitry.

2. Results

2.1. Optimal choice of GECI

With the aim of monitoring subcellular local Ca^{2+} domains, GECIs have been placed near the domain space by fusion to the cytosolic face of the Ca^{2+} channel itself [19–26] and likewise we focused on Ca^{2+} nanodomains generated by the lysosomal Ca^{2+} -permeable channel, TPC2 which is crucial for phagocytosis [19]. However, a systematic justification of which GECI to use has not been undertaken, and although the Ca^{2+} affinity of the reporter should match the amplitude range of the nanodomain $[\text{Ca}^{2+}]$, the latter is unknown and therefore cannot act as a guide. Hence, we evaluated different GECIs in order to optimize Ca^{2+} -nanodomain recordings, with a view to best match the local $[\text{Ca}^{2+}]$, minimize the Ca^{2+} spill-over from other Ca^{2+} sources and thereby selectively record the TPC2 Ca^{2+} -nanodomain.

When targeting Ca^{2+} reporters to the cytosolic face of the lysosome, we first selected a panel of six different GECIs of different colours and Ca^{2+} affinities (covering two orders of magnitude from 0.14 to 12 μM ; Table 1) and from different families (CaMPs and GECOs). We first

Table 1
Properties of published GECIs.

GECI	$K_d \text{ Ca}^{2+}$ (μM)	DR(fold)	n_H	Ref
Green GECIs				
GCaMP6s	0.14	63.2	2.9	[26]
GCaMP3	0.41	12.3	2.1	[71]
	0.66	12.0	nd	[77]
	0.26	12.3	3.1	[78]
	0.34	13.5	2.5	[26]
G-GECO1.2	1.2	23	2.1	[79]
	1.0	nd	nd	[19]
Orange/Red GECIs				
O-GECO1	1.5	146	2.1	[67]
RCaMP181	1.3	10.5	2.5	[71]
LAR-GECO1.2	12.0	8.7	1.4	[68]

Published properties of the different Ca^{2+} indicators used in this study. Parameters were determined in vitro for their unfused, cytosolic versions. DR = dynamic range, n_H = Hill Slope. Nd = not determined. RCaMP181 is also known as RCaMP1h [71]. Mean values of GCaMP3 were used for GECI calibration: K_d = 0.418 μM , DR = 12.5, n_H = 2.6.

verified that each GECI fusion-protein targets correctly to the lysosome in transiently transfected macrophages (RAW264.7 cells), as determined by their colocalization with a lysosomal marker (LAMP1 tagged with a complementary-colour fluorescent protein). Because the GECIs are dim at resting Ca^{2+} , images were collected immediately after saturating the GECI with high Ca^{2+} using 1 μM ionomycin/10 mM extracellular Ca^{2+} . Generally, TPC2 fusions localized consistently well to the lysosomes (Fig. 1A,B), with the exception of a commonly used pore-dead mutant, TPC2-L265P [21,27] which, in macrophages, was often retained in the ER (Fig. S1A,B). Only using correctly localized fusions, we then monitored their ability to record Ca^{2+} signals. Note that fusion of the GECI to TPC2 does not alter its Ca^{2+} affinity [19].

We recently showed that stimulation of the macrophage FcR recruits endo-lysosomal Ca^{2+} channels (TPC2 or TRPML1) to form local Ca^{2+} nanodomains [19]. These Ca^{2+} nanodomains were detected by a channel-GECI fusion but not by the unfused, cytosolic form of the GECI i.e. a lysosomal GECI location was key [19]. In view of this, our new screen compared the unfused form of each GECI as one control for spill-over of Ca^{2+} emanating from other sources (but see Fig. 3 for additional controls). All experiments were performed in Ca^{2+} -free medium to eliminate Ca^{2+} influx across the plasma membrane (Ca^{2+} -free medium was applied 1–2 min before imaging). In the first experiments, we activated the FcR with small (3- μm diameter) IgG-opsonized beads that couple to TPC2 (but not TRPML1), probably via NAADP [19]. Fig. 1C–H shows the responses of each GECI when either in the cytosol or as a TPC2-fusion; the amplitudes of the FcR-evoked Ca^{2+} signals are normalized to a subsequent ionomycin/ Ca^{2+} response (although non-normalized data showed the same trends – Fig.S1C). For each GECI, we quantified multiple parameters in situ, in order to gauge which GECI was the most sensitive and selective for monitoring lysosomal Ca^{2+} signals.

The first issue is to what degree do the TPC2-GECIs report the local Ca^{2+} nanodomain compared to the spill-over of Ca^{2+} from other cytoplasmic Ca^{2+} sources i.e. the *selectivity*. Selectivity is operationally defined as the TPC2-GECI detecting Ca^{2+} signals that the cytosolic GECI cannot i.e. the TPC2-GECI signals must exceed those in the cytosol. Selectivity was quantified as the ratio of the peak signals with the TPC2-fusion and cytosolic GECI. Although GCaMP6s exhibits the best in vitro dynamic range (Table 1), it was the least selective for FcR-stimulated nanodomains: the Ca^{2+} signals recorded by the TPC2-GCaMP6s were approximately the same amplitude as the cytosolic GCaMP6s (Fig. 1C,I, J). That is, the high-affinity (0.14 μM) GCaMP6s is almost saturated by even the *global* cytosolic FcR Ca^{2+} signals, regardless of whether the GECI is tethered to TPC2 or not; the higher local $[\text{Ca}^{2+}]$ of a nanodomain cannot then be observed on top of this, and GCaMP6s cannot be used to

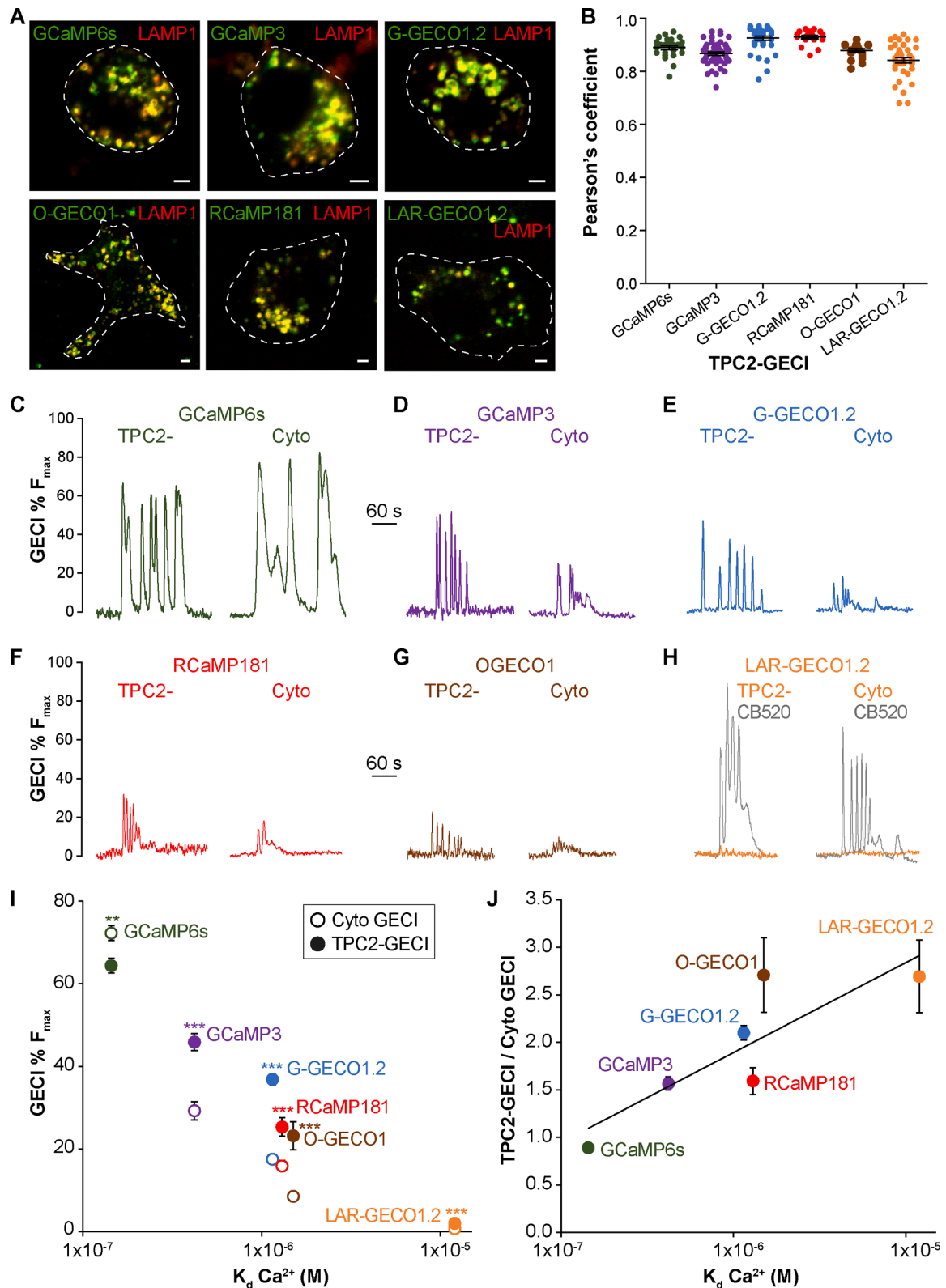


Fig. 1. Use of different GECIs to selectively monitor lysosomal Ca^{2+} signals.

(A) TPC2 GECI fusion-proteins (in green) were co-expressed with orthogonal LAMP1-mCherry or -mGFP (in red) in RAW264.7 macrophages; scale bar = 10 μ m. Co-localization (in yellow) indicates a lysosomal location and was quantified by (B) Pearson's coefficient. Each circle represents a single cell ($n = 19-44$ cells) with mean \pm SEM plotted. (C-H) Single-cell Ca^{2+} signals upon Fc γ R activation by opsonized 3- μ m beads in Ca^{2+} -free medium in RAW264.7 expressing either TPC2-GECI (TPC2-) or cytosolic GECI (Cyto). The % F_{max} was subsequently determined with 1 μ M ionomycin plus 10 mM Ca^{2+} , and traces normalized to this value. Global cytosolic Ca^{2+} was also monitored with cytosolic Calbryte indicators (shown only in H, CB520), to confirm responsiveness of the cells to beads. (I) Collated amplitudes of the first GECI spike from single-cells in C-H plotted as a function of their Ca^{2+} K_d . Data are mean \pm SEM of $N = 4-10$ experiments, $n = 40-260$ cells. *** $P < 0.001$, ** $P < 0.01$ significance determined by a paired t -test comparing each Cyto and TPC2-fusion GECI pair. (J) Selectivity was quantified by plotting the ratio of the TPC2-fusion and cytosolic GECI pair and plotted against their K_d .

selectively detect lysosomal Ca^{2+} domains.

In contrast, all the lower-affinity GECI fusions exhibited selectivity over the cytosolic forms, albeit to different extents. The lowest affinity (12 μM) red LAR-GECO1.2 only recorded FcR Ca^{2+} signals very poorly, whether as the cytosolic or TPC2-fusion version (Fig. 1H,I,J). This was not because FcR signals were absent in the transfected cells since they were detected by simultaneously recording the cytosolic Ca^{2+} with higher-affinity, green Calbryte520 (Fig. 1H); nor was this absence of signal due to non-functioning LAR-GECO1.2 because ionomycin/ Ca^{2+} was used as a positive control at the end of the experimental run. Our interpretation is that the physiological Ca^{2+} changes (global or lysosomal) are generally smaller than the useful detection range of this reporter ($\sim 1\text{--}100\ \mu\text{M}$), but the peaks are reported in a subset of cells where larger Ca^{2+} spikes happen to be generated (% LAR-GECO1.2 responders: cytosolic 43%, TPC2, 66%; the other GECIs average 86%). In such cells, the TPC2-LAR-GECO1.2 fusion showed larger Ca^{2+} responses than the cytosolic version (Fig. 1I,J). Indeed, it showed the highest discrimination between TPC2-tethered and cytosolic.

The remaining GECIs (Table 1), whose affinities were intermediate between GCaMP6s and LAR-GECO1.2, showed better detection efficiencies but different selectivities. The rank order of selectivity for lysosomal signals was LAR-GECO1.2 > G-GECO1.2 \approx O-GECO1 > GCaMP3 \approx RCaMP181 > GCaMP6s as judged by the ratio of lysosomal and cytosolic signals (Fig. 1I,J). Plotting the lysosome/cytosolic ratio of the different GECIs as a function of the $\log_{10}K_d$ revealed a quasi-linear correlation (Fig. 1J): as the affinity drops, the selectivity improves, as would be expected for the selective detection of a higher local $[\text{Ca}^{2+}]$.

One potential criticism of our 'affinity' argument is that we have compared entirely different GECIs. Therefore, we re-engineered one single GECI (G-GECO1.2) to alter its K_d , not just with a view to reproducing the K_d shifts above, but also with the aim of titrating the K_d to better select between the local Ca^{2+} nanodomain and the cytosol. Therefore, we introduced single point mutations in the G-GECO1.2 calmodulin (CaM), the Ca^{2+} -binding site domain of this GECI, known to correspond to modest Ca^{2+} -affinity shifts [28]. We made three new GECIs, each with a single point-mutation (numbering corresponds to human CaM: N98S, A103V, and F90L; Fig. 2A) and determined their Ca^{2+} affinities in vitro using recombinant purified proteins. Compared to the WT G-GECO1.2, the N98S and A103V versions each gave a modest decrease in affinity whereas the F90L conferred the greatest (4.7-fold) decrease in affinity (Fig. 2B,C). Note that in this assay, the WT G-GECO1.2 absolute affinity was slightly lower than published values (Table 1), but the mutations show relative affinity shifts.

We then transfected macrophages with cytosolic or TPC2-fused G-GECO1.2 variants and since they all correctly localized to lysosomes (Fig. S1E,F) we could monitor FcR responses as before. Note that none of the 'affinity' point-mutations substantially impacted the in situ dynamic range compared with WT G-GECO1.2 (Fig. S1D). When comparing the cytosolic and TPC2-fused GECI responses, the channel-fusions all exhibited a greater fluorescence change than the soluble GECIs, as anticipated (Fig. 2D-G). Most importantly, the relationship between the responses and K_d of the G-GECO1.2 mutants showed the same trends as previously observed with the panel of different types of GECI i.e. the selectivity (TPC2/cytosol) ratio improved as the K_d was increased (Fig. 2H,I).

Both GECI panels revealed an additional important aspect. As the GECI affinity is lowered, the improved local/global selectivity ratio comes at the price of a reduced ability to record local events (lower amplitudes). This trend held for both the different types of GECI (Fig. 1I) and the G-GECO1.2 mutants (Fig. 2H). That is, local domains were recorded at the lower end of the $[\text{Ca}^{2+}]$ /fluorescence curves of the mutants such that, for example, a 30% improvement in selectivity came at a penalty of a 50% reduction in the TPC2-G-GECO1.2 signal. In view of this, the optimal GECI Ca^{2+} affinity is $\sim 1\ \mu\text{M}$ and even slight shifts in the affinity reduce the detection efficiency. Therefore, the optimal reporter for TPC2 Ca^{2+} nanodomains is the original G-GECO1.2 [19].

2.2. Lysosome Ca^{2+} -nanodomain architecture

Having affirmed G-GECO1.2 as the optimal GECI, we used it to define the nature of the Ca^{2+} nanodomain. Recently, we showed that TPC2-G-GECO1.2 signals were absolutely dependent on the activity of the TPC2 channel but not on global Ca^{2+} signals i.e. they persisted even when other Ca^{2+} sources (Ca^{2+} influx, ER- Ca^{2+} release) were eliminated [19], strongly implying that TPC2-G-GECO1.2 detects lysosomal Ca^{2+} nanodomains. However, a confounding factor is that the expression of TPC2-G-GECO1.2 not only locates the G-GECO1.2 within the Ca^{2+} nanodomain, but it also increases the number of TPC2 channels. We therefore asked if the large signals observed with TPC2-G-GECO1.2 were simply due to TPC2 overexpression driving a greater global Ca^{2+} response. We addressed this concern in multiple ways.

First, we monitored the unfused cytosolic G-GECO1.2 signal in cells co-expressing TPC2-mCherry, thereby divorcing the effect of expression levels from G-GECO1.2 location. Although there was a small enhancement of the cytosolic G-GECO1.2 response by TPC2 over-expression (Fig. 3A), it did not reproduce signals observed with the fusion TPC2-G-GECO1.2 (Fig. 3B). This agrees with our previous data showing that TPC2 over-expression only modestly enhanced the signals of the cytosolic Calbryte-590 Ca^{2+} -dye (whose affinity is similar to that of G-GECO1.2) [19], and reinforces the notion that the G-GECO1.2 has to be fused to the TPC2 to detect local domains.

Second, since a lysosomal location of G-GECO1.2 is important for selective detection, we asked whether the G-GECO1.2 had to be fused to TPC2, or if it was sufficient to be tethered to the cytosolic face of the lysosome in other ways. Therefore, we fused G-GECO1.2 to the lysosomal marker, LAMP1 (which localized correctly; Pearson's coefficient 1.06 ± 0.20 , $n = 40$ cells, Fig. S1G); because LAMP1 is not itself a channel, the fused G-GECO1.2 will only detect Ca^{2+} released by either those adjacent channels on the lysosome or those more remote on the ER, such as IP₃Rs [25]. Upon activating the FcR, LAMP1-G-GECO1.2 recorded robust Ca^{2+} signals, notably larger than the equivalent cytosolic G-GECO1.2 (Fig. 3C), but smaller than the TPC2-G-GECO1.2 (Fig. 3B). This indicates that LAMP1-G-GECO1.2 detects peri-lysosomal Ca^{2+} responses that the cytosolic version cannot. We investigated this further.

For it to record larger signals, LAMP1-G-GECO1.2 must be a bystander close to endogenous high Ca^{2+} nanodomains, and these can come from two sources: either they are generated by adjacent lysosomal Ca^{2+} channels, or by closely apposed ER Ca^{2+} -channels at privileged lysosome-ER junctions [25]; both are possible since the FcR stimulates both lysosomal and ER Ca^{2+} signalling [19]. If lysosomal channels are the source, then channel over-expression should enhance the FcR response and, indeed, when TPC2-mCherry was co-expressed, the LAMP1-G-GECO1.2 responses were enhanced (Fig. 3C); this required an active TPC2 channel because expression of an inactive, pore-dead mutant (TPC2-D276K-mCherry) [19,29] did not enhance the LAMP1-G-GECO1.2 signal (Fig. 3C). This can only be detecting local lysosomal Ca^{2+} because TPC2-mCherry does not augment the global cytosolic G-GECO1.2 response to the same degree (Fig. 3A). Note that overexpression of TPC2 did not alter the lysosomal/cytosolic G-GECO1.2 ratio (Figs. 3A,C), i.e. the LAMP1-G-GECO1.2 selectivity was the same for endogenous and ectopic TPC2 (lysosome/cytosol ratio: mCherry, 1.69 ± 0.11 ; TPC2-mCherry 1.79 ± 0.08 ($P > 0.05$)).

Next, we assessed whether the source of the Ca^{2+} was from ER-resident IP₃Rs e.g. recruited by Ca^{2+} induced Ca^{2+} release at local privileged lysosome-ER membrane contact sites [25]. To test this, we stimulated macrophages with the purinoceptor agonist, UTP, which only couples to IP₃ and not to TPC-dependent Ca^{2+} signalling [19,30]. With UTP, the LAMP1-G-GECO1.2 response was no different from the cytosolic G-GECO1.2 alone (Fig. 3D,E) meaning that it only detected the global spill-over and not any privileged lysosome-IP₃R local Ca^{2+} . Finally, even in cells co-expressing LAMP1-G-GECO1.2 and TPC2-mCherry, UTP failed to mimic the TPC2-G-GECO1.2 response to

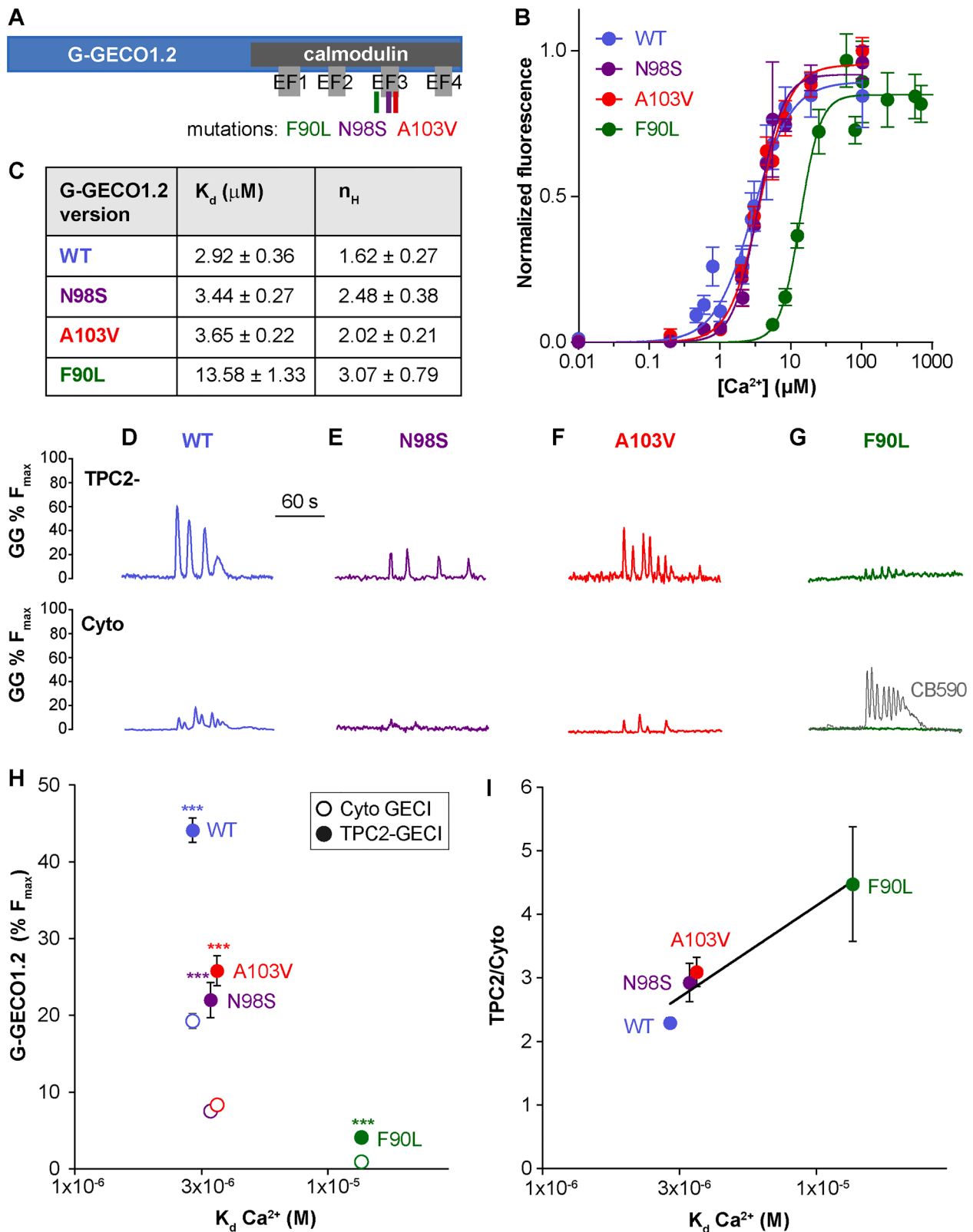


Fig. 2. Impact of different-affinity G-GECO1.2 mutants on TPC2 Ca²⁺ signals.

(A) Cartoon of the three separate single point-mutations (N98S, A103V and F90L) within the calmodulin motif of G-GECO1.2. (B-C) The affinity of recombinant soluble G-GECO1.2 protein (wildtype, WT and mutant forms) for Ca²⁺ (K_d) and Hill slopes (n_H) were calculated from the plots in (B), *N* = 3–8 experiments. (D-G) The TPC2-fused and cytosolic versions of G-GECO1.2 were compared in response to FcγR activation with opsonized 3-μm beads in Ca²⁺-free medium in RAW 264.7; single-cell traces normalized to the respective G-GECO1.2 F_{max}. (H) Collated amplitudes of the first Ca²⁺ spike from single-cells in D-G plotted as a function of the Ca²⁺ K_d determined in C. Data are mean ± SEM of *N* = 3–8 experiments, *n* = 52–273 cells. (I) The lysosome/cytosolic ratio of the different G-GECO1.2 s as a function of their Ca²⁺ K_d.

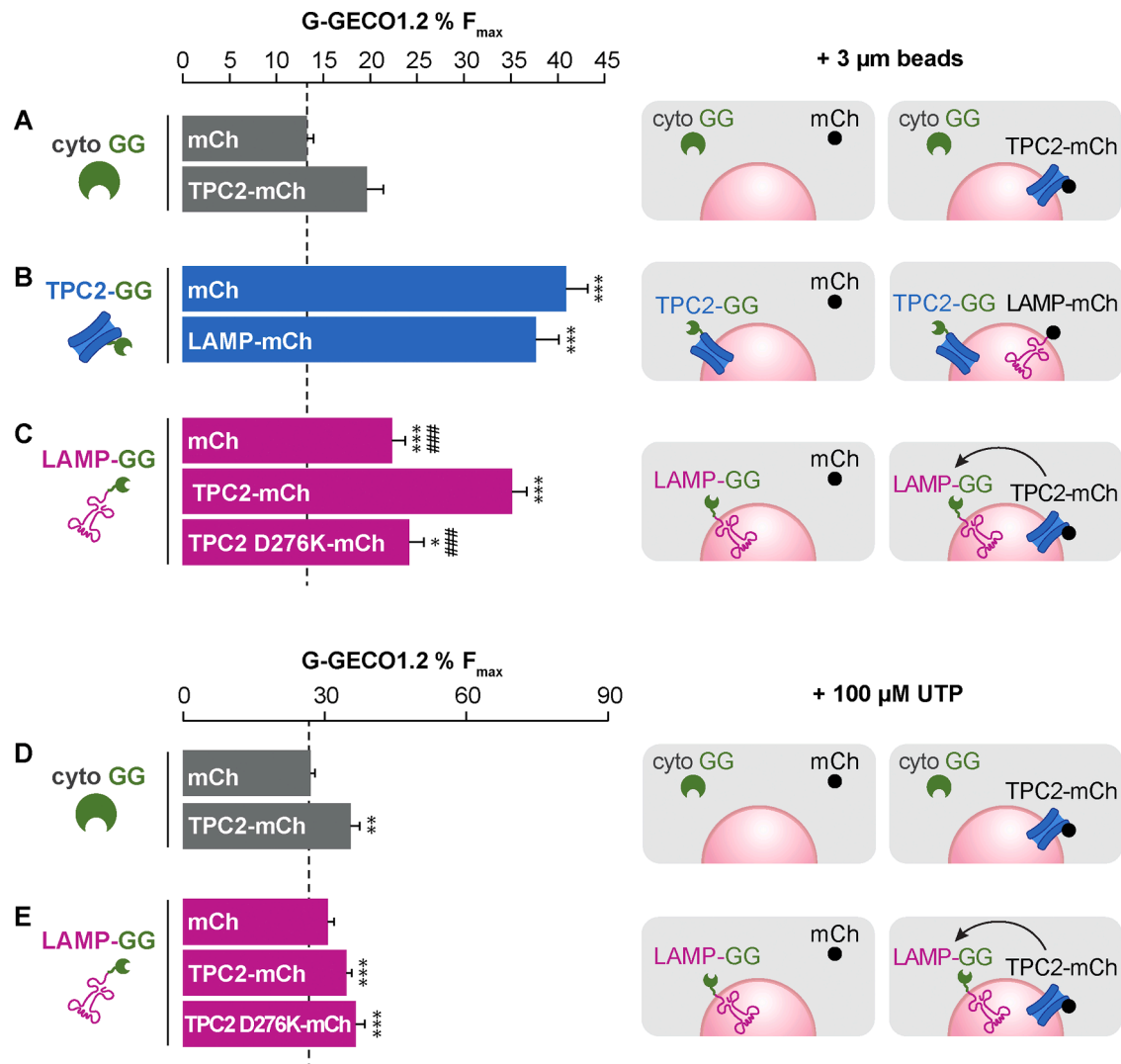


Fig. 3. GEC1 fusion to an activated TPC2 is obligatory for detecting TPC2 Ca^{2+} nanodomains.

Collated mean \pm SEM of the first Ca^{2+} amplitude upon FcγR activation with opsonized 3 μm beads in RAW264.7 in Ca^{2+} -free medium, detected using G-GECO1.2 versions: (A) cytosolic (cyto GG), (B) TPC2-tethered (TPC2-GG), and (C) LAMP1-fusion (LAMP-GG). Data are normalized to the maximum G-GECO1.2 (F_{max}) response to 1 μM ionomycin plus 10 mM CaCl_2 . The labels on the graph bars denote the dual expression in a single cell of soluble mCherry (mCh), LAMP1 fused to mCherry (LAMP-mCh) or mCherry fusions with wildtype TPC2 (TPC2-mCh) or the pore-dead mutant (TPC2 D276K-mCh) with the G-GECO1.2 versions. The cartoons on the right depict the dual expression. $N = 5$ –13 experiments and $n = 42$ –230 cells; significance determined by ANOVA *** $P < 0.001$, * $P < 0.05$ vs cytosolic G-GECO1.2 + mCh; ### $P < 0.001$ vs LAMP-GG + TPC2-mCh. (D-E) As in A and C, but RAW264.7 macrophages were stimulated with 100 μM UTP. $N = 4$ –6 experiments, $n = 46$ –154 cells; *** $P < 0.001$, ** $P < 0.01$ vs cytosolic G-GECO1.2 + mCh.

FcγR engagement (Fig. 3D,E), and the minor effect of TPC2-mCherry was non-specific because it was no different to pore-dead TPC2-D276K-mCherry (Fig. 3E).

Taken together, the data further strengthens our assertion that, in RAW264.7 cells, the large TPC2-G-GECO1.2 signals are authentically due to TPC2 Ca^{2+} nanodomains and not due to Ca^{2+} spilling over from the cytosol (ER) [19]. Moreover, LAMP1-G-GECO1.2 detects Ca^{2+} released from adjacent TPC2 (be it endogenous or over-expressed) and not from Ca^{2+} transfer from adjacent ER. This implies a proximity between TPC2 and LAMP1.

2.3. Lysosomal Ca^{2+} channels act autonomously

These LAMP1-G-GECO1.2 experiments revealed that this protein lay close to endogenous TPC2 and sensed some of the endogenous Ca^{2+} nanodomain that spilled over. In view of this, we wondered if another lysosomal protein, the Ca^{2+} channel, TRPML1, was exposed to TPC2 spill-over Ca^{2+} or not. This is physiologically crucial because, in a form

of extreme lysosomal compartmentation, TPC2 and TRPML1 are differentially activated and couple to very different downstream processes at phagocytosis [19,20]. We have hypothesised that these channels act independently by generating their own unique Ca^{2+} nanodomains that couple to their cognate Ca^{2+} decoders, but for this model to work, each channel's Ca^{2+} nanodomain must be insulated from the other. We therefore tested if activation of one channel family spilled over onto the other family.

In the following experiments, we activated the endogenous channel via the physiological FcγR pathway and monitored whether the Ca^{2+} that is released could be sensed by the G-GECO1.2-fusion of the other (analogous to the LAMP1-G-GECO1.2, Fig. 3C). In cells expressing TRPML1-G-GECO1.2, 3- μm beads activate endogenous TPC2 (but not TRPML1; Fig. 4A) [19]. Although Ca^{2+} signals were weakly detected by TRPML1-G-GECO1.2, these small signals simply reflected Ca^{2+} spill-over from the cytosol, because they were the same amplitude as those recorded with unfused cytosolic G-GECO1.2 (Fig. 4B,D). That is, in contrast to LAMP1-G-GECO1.2 (Fig. 3), TRPML1-G-GECO1.2 did not

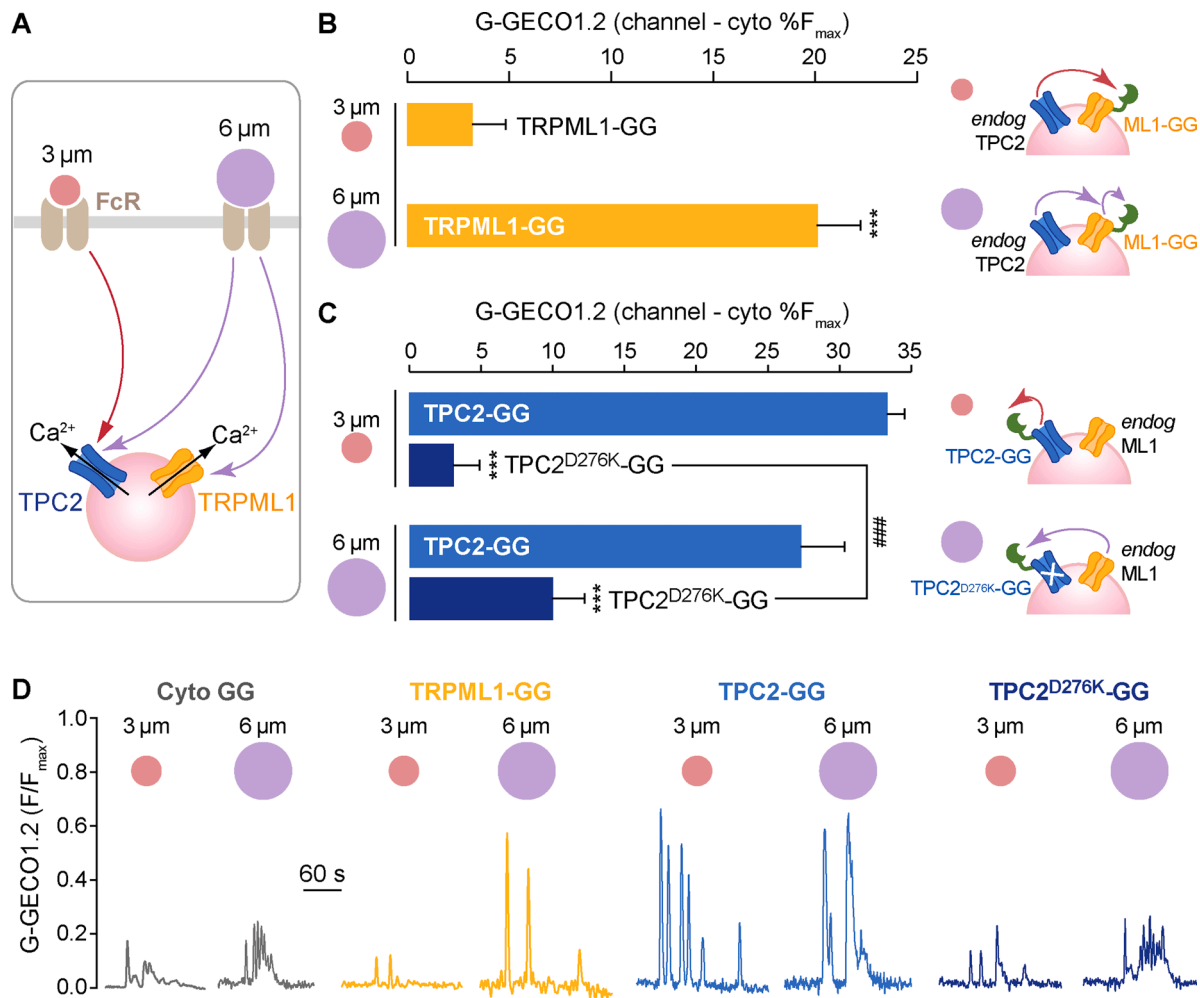


Fig. 4. TPC2 and TRPML1 channels generate independent Ca²⁺ nanodomains.

Ca²⁺ release from endogenous channels was evoked by either 3-μm or 6-μm opsonized beads and neighbouring channel-G-GECO1.2 fusions recorded the degree of spill over. (A) Cartoon illustrating which lysosomal channels are activated by different-sized beads. Single-cell Ca²⁺ changes expressed as the response over and above the cytosolic G-GECO1.2 global background i.e., quantified as the (Peak – basal) with the mean cytosolic G-GECO1.2 responses (panel D) subtracted from all values. (B) Negligible spill over from endogenous TPC2 onto TRPML1-G-GECO1.2 (3-μm), whereas 6-μm beads directly activate TRPML1-G-GECO1.2 channels. (C) 3-μm beads directly activate TPC2-G-GECO1.2 but not the pore-dead TPC2-D276K-G-GECO1.2. 6-μm beads directly activate TPC2-G-GECO1.2, whereas TPC2-D276K-G-GECO1.2 weakly detects some spill-over from the activation of endogenous TRPML1. Bar charts express the mean ± SEM of 69–78 cells, *N* = 4 (B) and 34–220 cells, *N* = 3–8 (C). (D) Representative single-cell traces of experiments in (B, C) stimulated by different sized beads (labelled by the corresponding schematic above).

detect a privileged local Ca²⁺ response emanating from TPC2. As a positive control, FcR activation with larger 6-μm beads recruits TRPML1, and local Ca²⁺ nanodomains are detected with the TRPML1-G-GECO1.2 which are bigger than the cytosolic G-GECO1.2 (Fig. 4B,D) [19]. The data with 3-μm beads therefore indicates that TRPML1 is too far away from TPC2 to be cross-contaminated by the endogenous TPC2 Ca²⁺ nanodomain.

The complementary (reverse) configuration was tested next i.e. does activation of endogenous TRPML1 spill over onto TPC2? This was not as experimentally tractable as the converse configuration because there is no known physiological stimulus in macrophages that exclusively couples to TRPML1; whilst 6-μm beads do activate TRPML1, they co-activate TPC2 (Fig. 4A) [19], meaning we cannot monitor spill over onto TPC2-G-GECO1.2 because Ca²⁺ would also be egressing the open TPC2. Instead, we used the pore-dead TPC2-D276K-G-GECO1.2 because it does not itself conduct Ca²⁺ and does not generate its own Ca²⁺ nanodomain but it should nonetheless be able to detect Ca²⁺ spill-over from TRPML1. Application of 6-μm beads activates endogenous TRPML1 (Fig. 4B,D) but a signal was only weakly detected by TPC2-D276K-G-GECO1.2 (Fig. 4C,D). Quantitatively, TPC2-D276K-G-GECO1.2 was picking up some local lysosomal Ca²⁺

spill-over because it was slightly bigger than the cytosolic G-GECO1.2 alone (Fig. 4C,D). However, this bystander effect was far smaller than the Ca²⁺ nanodomain normally self-generated upon activation of wild-type TPC2, as shown with 6-μm beads and TPC2-G-GECO1.2 (Fig. 4C,D). In other words, physiological activation of endogenous TRPML1 only weakly cross-contaminated TPC2 channels and could not reproduce the large Ca²⁺ nanodomain that TPC2 activation itself evoked (see Discussion).

Together, the data indicate that Ca²⁺ channels on the lysosome do not generate a broad peri-vesicular halo of Ca²⁺, but rather produce discrete hot-spots around the surface (Fig. 6F). That is, whichever channel family is stimulated, the other channel family is largely insulated from those Ca²⁺ changes. The two channel families demonstrably generate their own autonomous Ca²⁺ nanodomains and provides a framework for channels on the same small lysosome to selectively couple to different physiological processes.

2.4. Calibrating [Ca²⁺] nanodomains

The absolute magnitude of lysosomal Ca²⁺ nanodomains has not been determined in any system, to the best of our knowledge.

Fortuitously, we were perfectly positioned to convert our fluorescence data into $[Ca^{2+}]$ by exploiting a previous mathematical approach [31]: when the same biological Ca^{2+} response is monitored with different-affinity GECIs (an ‘affinity ladder’, Fig.S2A), simultaneous equations can be solved to obtain the absolute $[Ca^{2+}]$ (see Methods). This approach conveniently obviates common errors of estimating F_{min} and F_{max} in situ with Ca^{2+} ionophores. As detailed in the Methods, the responses to a selected pair of GECIs are compared and the equation returns both a basal and a peak $[Ca^{2+}]$. This is then repeated for all the pairing permutations, i.e., 6 GECIs return 15 paired values of basal and peak $[Ca^{2+}]$ (Fig. 5A; Fig. S2B).

When applied to the first panel of different GECI families, the cytosolic peak $[Ca^{2+}]$ was $\sim 0.5 \mu M$ and the TPC2 nanodomain $\sim 0.7 \mu M$ (Fig. 5A), and the $\Delta[Ca^{2+}]$ response (peak-basal) was approximately two-fold larger in the nanodomain compared with the cytosol ($P < 0.001$). We applied the same analysis to the second panel (the G-GECO1.2 variants) and reassuringly obtained a similar pattern (Fig. 5B; Fig. S2C), albeit shifted in absolute values because we used our recombinant-protein affinities which were slightly higher: the peak $[Ca^{2+}]$ of the TPC2 nanodomain was $\sim 2.1 \mu M$, whilst the $\Delta[Ca^{2+}]$ changes remained around two-fold different between cytosolic and TPC2 nanodomain (Fig. 5B). Therefore, TPC2-GECI fusions report only a two-fold difference between global and reported local $[Ca^{2+}]$ changes, with peak TPC2-G-GECO1.2 values of $0.7\text{--}2.1 \mu M$.

These surprisingly low values (and narrow selectivity-window over the cytosolic signal) prompted us to evaluate the nanodomain measurements in more detail and ask why they might appear to be closer to the cytosolic $[Ca^{2+}]$ than expected. A major factor determining the $[Ca^{2+}]$ value returned by a GECI is its proximity to the mouth of the channel pore because the $[Ca^{2+}]$ falls off steeply with distance from the source [2,32,33]. This has not, to date, been accounted for. To estimate this distance in our system, we need to know the structures of the TPC2-G-GECO1.2 dimer. We engineered the GECIs at the C-terminus of TPC2 but this tail was not determined in the Cryo-EM structure which is of a truncated TPC2 dimer [34]. Therefore, we used ColabFold [35] to model the full-length protein, and the core structure was reassuringly similar to the Cryo-EM (RMSD = 0.888 \AA) (Fig.S3A). Note that the model suggested that this ‘missing’ C-tail was relatively unstructured (red portion, Fig.S3A,B). We first modelled the TPC2-G-GECO1.2 fusion, and whilst the TPC2 helices were well predicted, the C-terminal GECI structure was only partially accurate (Fig.S3C), so we needed a different approach. Instead, we modelled the unfused G-GECO1.2 with its Linker that connected the GECI to the TPC2 C-tail and predicted a structure that was in better agreement with the crystal structure of closely related R-GECO1 (Fig.S3A): the predicted and empirical CaM domains overlapped (RMSD of 0.974 \AA) although the cpGFP domain was rotated $\sim 90^\circ$ relative to the CaM but otherwise well modelled when explicitly fitted to the crystal beta-barrel (RMSD of 0.906 \AA), except for a small section that detached from the main barrel (see orange region of cpGFP in the middle Linker-G-GECO1.2 panel of Fig.S3A). Note that the Linker was also unstructured. We then fused this more accurate G-GECO1.2 model to the full-length TPC2 model in silico to obtain multiple TPC2-G-GECO1.2 models that varied the bond flexion angle at the attachment point and, therefore, the pore-GECI distance (see Methods).

When the GECI was attached in extended conformations (Fig. 5C), we measured the distance between the closest residues of each of the four EF-hands of CaM and the Arg704 of TPC2, arbitrarily used as a marker adjacent to the pore mouth. Across 3 models, we found that the distances were $7.6 \pm 0.9 \text{ nm}$ for the N-terminal EF hands and $9.3 \pm 0.3 \text{ nm}$ for the C-terminal equivalents. Overall, the mean EF-hand to pore distance was $8.5 \pm 0.6 \text{ nm}$ in these extended conformations.

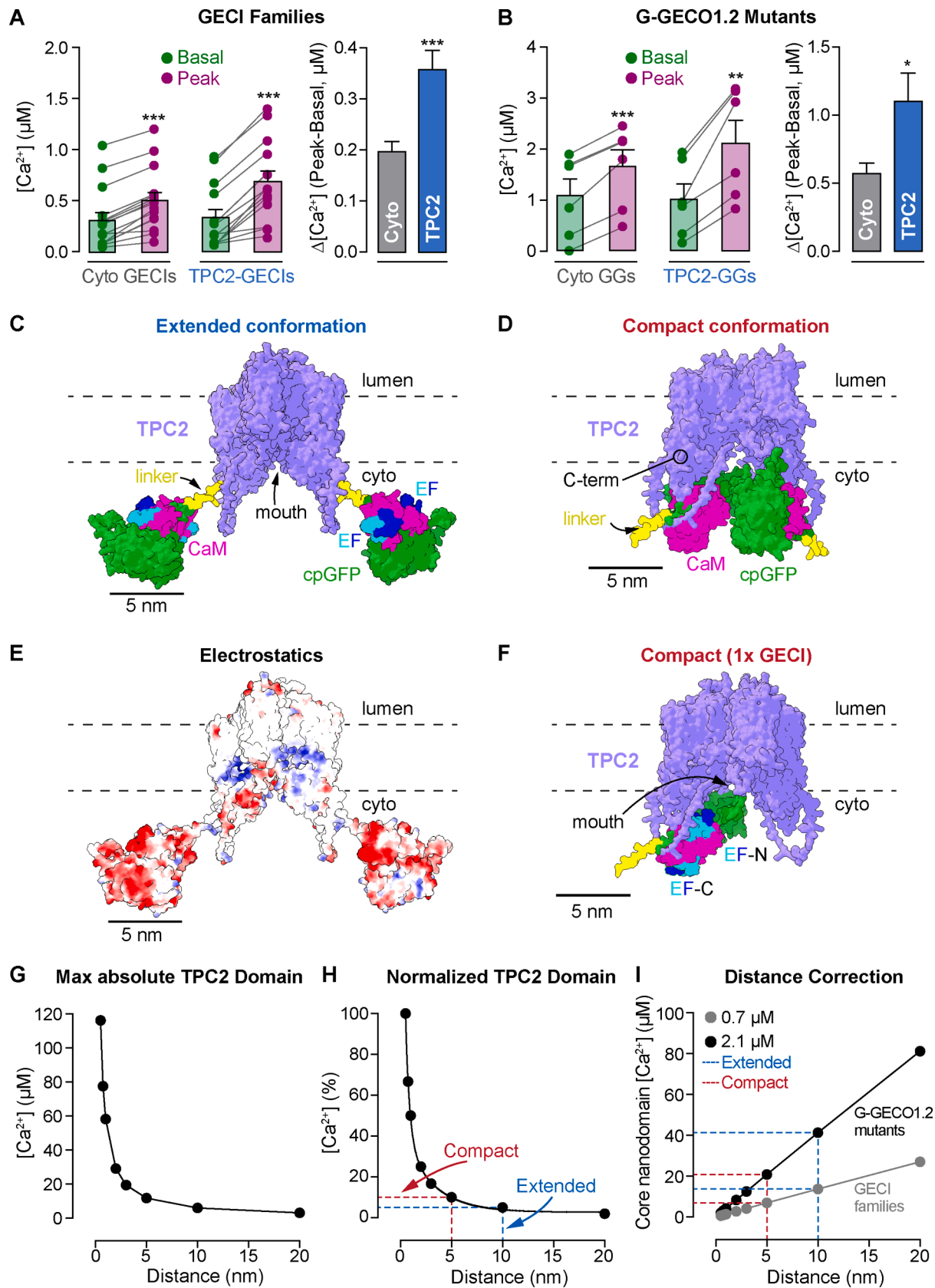
However, we cannot ignore that both the TPC2 C-tail and the Linker appear to be unstructured and flexible, in which case the Tail-Linker might, in an extreme instance, bend back on itself and place the GECI close to the channel ‘funnel’. To account for this scenario, we manually placed two copies of the GECI (one for each TPC2 monomer) as close as

possible to the mouth of the channel with the Linker facing outward towards the TPC2 C-tail (Fig. 5D,F). Because the pair of cpGFP domains obstruct access, the EF hands are still at some distance; the N-terminal EF-hand closest distance (Asp342) was $\sim 3 \text{ nm}$ whereas the distal, C-terminal EF-hand (Gly414) was $\sim 8 \text{ nm}$ away (an average of 5.5 nm). These values represent the minimum distances of the GECI from the pore that can be sterically accommodated. We would argue, however, that the likelihood of both copies of G-GECO1.2 being placed in this conformation is low, not just because this is a restricted space, but also because the surface charges of the G-GECO1.2 are predominantly negative (Fig. 5E), and inter-molecular repulsion would not favour a compacted conformation. Nevertheless, we include these values as a minimum guide.

Theoretically, then, the Ca^{2+} -binding sites of G-GECO1.2 could be approximately located anywhere between 5 and 10 nm from the TPC2 pore. $[Ca^{2+}]$ falls off steeply with distance from the pore and Neher modelled the spatial profile of a local Ca^{2+} domain by calculating the net $[Ca^{2+}]$ outcome from the rates of Ca^{2+} egress from the channel and Ca^{2+} diffusion into the bulk cytosol [2,33,36]. Using the single-channel properties of human TPC2 [37] we calculated the maximum single-channel current (see Methods) and, using this model, we derived a theoretical spatial profile of the TPC2 Ca^{2+} nanodomain which predicted a maximum nanodomain $[Ca^{2+}]$ of $\sim 116 \mu M$ (Fig. 5G). In order to distance-adjust our calibrated GECI values, we normalized the TPC2 profile to the maximum core nanodomain $[Ca^{2+}]$ (Fig. 5H). It is crucial to note that this curve is independent of the absolute current, i.e., when we used different P_o values to derive Ca^{2+} -nanodomain profiles over vastly different $[Ca^{2+}]$ ranges (Fig. S4A), the curves normalized to the respective maximal $[Ca^{2+}]$ are superimposable (Fig. S4B). Therefore, our distance correction is entirely unaffected by potential errors in the single-channel current used.

Fig. 5H shows that, by 5 nm (compact) and 10 nm (extended conformation), the local $[Ca^{2+}]$ can have fallen to 10% and 5% of the channel-mouth value respectively, even at steady state [2,33,36]. Therefore, when the GECI reports a $[Ca^{2+}]$ of 0.7 or $2.1 \mu M$, we can calculate the equivalent core nanodomain $[Ca^{2+}]$ as a function of the GECI distance from the pore (Fig. 5I). Hence, the TPC2 core nanodomain $[Ca^{2+}]$ is extrapolated to be $7\text{--}21 \mu M$ (if G-GECO1.2 is 5 nm from the mouth) or $14\text{--}42 \mu M$ (if 10 nm away) (Fig. 5I). Even with our conservative GECI-pore distance estimates, the upper nanodomain $[Ca^{2+}]$ of $42 \mu M$ determined empirically in situ compares with the Neher mathematical model of the theoretical maximum of $\sim 116 \mu M$. A sub-maximal P_o of ~ 0.005 (equivalent to a single-channel current of 0.013 pA), more closely corresponds to the core $[Ca^{2+}]$ of $\sim 40 \mu M$ that we have determined empirically (Fig. S4A-C).

Experimental support for the Ca^{2+} -nanodomain spatial profile was revealed by the effect of Ca^{2+} chelators upon the TPC2-G-GECO1.2 response. EGTA and BAPTA are chelators that bind Ca^{2+} with slow and fast kinetics respectively, and BAPTA is unique in its ability to buffer Ca^{2+} closer to the channel mouth, whereas EGTA is less effective [2,32]. This is confirmed theoretically by modelling the Ca^{2+} nanodomain in the presence and absence of these chelators [32]: $1\text{--}10 \text{ mM}$ EGTA had little effect upon the Ca^{2+} nanodomain profile up to 50 nm from the channel mouth, whereas the equivalent BAPTA concentrations suppress the Ca^{2+} nanodomain (Fig. 6A-C; Fig. S4D-H). Experimentally, loading the cytosol of RAW264.7 cells with either EGTA or BAPTA had different effects upon the TPC2-G-GECO1.2 recordings (Fig. 6D,E). The local TPC2-G-GECO1.2 response remained largely unaffected by the presence of EGTA, even though EGTA inhibited the global- Ca^{2+} response monitored simultaneously with cytosolic Calbryte-590 (Fig. 6D,E) as we observed previously [19]. In contrast, the local TPC2-G-GECO1.2 responses were inhibited by BAPTA loading, in parallel with the repression of the global cytosolic Ca^{2+} responses (Fig. 6D,E). That is, in agreement with the modelling, EGTA was unable to collapse the Ca^{2+} nanodomain whereas BAPTA was highly effective, thereby strengthening the notion that the TPC2-G-GECO1.2 is monitoring local Ca^{2+} nanodomains within



(caption on next page)

Fig. 5. Calibration of the absolute $[Ca^{2+}]$ of the nanodomain accounting for the GECI distance from the channel mouth.

(A) Data from the different GECI types in Fig. 1 were converted to absolute $[Ca^{2+}]$ using the pairwise-calibration method which returns a Basal and Peak value for each GECI-pair comparison (displayed as individual paired points connected by a line). The Basal and Peak are absolutes, whereas the delta is the paired Peak minus Basal. (B) An identical calibration was performed using the data of Fig. 2 derived from G-GECO1.2 mutants. Bar charts are the mean \pm SEM of 15 and 6 determinations respectively. A paired *t*-test was used to compare Basal and Peak, whereas an unpaired *t*-test compared the Cyto and TPC2 Delta values. * $P < 0.05$, ** $P < 0.01$, *** $P < 0.001$. (C-F) Molecular models of TPC2-G-GECO1.2 fusion protein generated by ColabFold and ChimeraX. (C) Surface model of the in silico fusion of TPC2-linker-G-GECO1.2 dimer in an Extended conformation. The TPC2 dimer (purple), linker (yellow), CaM (magenta) with the EF-hand pairs of each lobe coloured as blue (1st) and cyan (2nd), circularly permuted GFP (cpGFP, green). (D) Compact conformation (minimum distance between GECI and the TPC2 pore) generated by manually placing each soluble GECI EF-hand as close as possible to the pore in a head-to-head configuration. (E) Surface-model of the surface electrostatic charge of the dimer where acidic residues are red, and basic residues are blue. (F) Same Compact model as in D, but with one copy of the G-GECO1.2 removed to better reveal the position of the EF hands. Scale bars represent 5 nm. (G) Neher model of the spatial profile of a local Ca^{2+} domain, with the maximum absolute $[Ca^{2+}]$ plotted against the distance from the mouth of the channel pore using the maximum TPC2 single-channel Ca^{2+} flux calculated in the Methods. (H) Neher model of the spatial profile of the Ca^{2+} nanodomain normalized to the maximum $[Ca^{2+}]$. (F) The effect of the GECI-pore distance upon the calculated $[Ca^{2+}]$ in the core nanodomain. The calibrated TPC2 peak $[Ca^{2+}]$ was either taken as 0.7 μM (grey) or 2.1 μM (black).

the theoretical dimensions.

In summary, the Ca^{2+} -binding sites of the GECIs cannot be accommodated at the core of the Ca^{2+} nanodomain at the mouth of the channel but are more likely to be physically placed at the edge of the TPC2 Ca^{2+} nanodomain (Fig. 6F). As such, they will be underestimating the point-source Ca^{2+} nanodomain by at least 10- to 20-fold (7–42 μM), which means that the local lysosomal change will exceed the cytosolic peak $[Ca^{2+}]$ (~0.5 μM) by up to 2 orders of magnitude. These values represent the first empirical estimates of lysosomal Ca^{2+} nanodomains in any system.

3. Discussion

3.1. Optimizing lysosomal GECIs

In line with others [38], we distinguish a Ca^{2+} nanodomain from a Ca^{2+} microdomain by the former's being selectively inhibited by fast BAPTA but not by slow EGTA. In macrophages, FcR-mediated, TPC2-dependent phagocytosis is only inhibited by BAPTA, and not by EGTA [19] and thereby implied that the local TPC2 Ca^{2+} signal is both a nanodomain and of functional importance. A Ca^{2+} nanodomain is suggested to be about ten-fold higher than a microdomain, e.g. ~100 μM versus 1–5 μM [38], but, to date, no one has determined absolute $[Ca^{2+}]$ values of any local lysosomal Ca^{2+} domain which became one goal of this study using channel-GECI fusions.

The literature contains examples of Ca^{2+} -permeable endo-lysosomal channels fused to different GECIs but often without a justification of the choice of GECI and an assumption that the construct specifically monitors lysosomal Ca^{2+} nanodomains merely on the basis of its localization. In view of this uncertain basis for use, we undertook a systematic analysis of 9 different GECIs fused to TPC2 in order to understand what aspects are important for selective nanodomain recording and what factors restrict their practical usefulness. To date, workers have aimed to monitor local Ca^{2+} nanodomains by fusing endo-lysosomal proteins to an array of mostly green GECIs including — but not limited to — GCaMP6s [21], GCaMP6m [22], GCaMP3 [20], GCaMP5 [23], GCaMP7 [24], and G-GECO1.2 [19,25]. Their Ca^{2+} affinities and dynamic ranges differ significantly (Table 1), so what properties make for the best?

We exploited FcR-linked activation of TPC2 [19] as a physiologically important platform for testing a panel of channel-GECI fusions with different colours, dynamic ranges, and affinities (0.14 to 12 μM). Ultimately, a major conclusion is that the higher the Ca^{2+} affinity, the worse was the selectivity for lysosomal Ca^{2+} over the signals from other Ca^{2+} sources; GCaMP6s (K_d 0.14 μM) showed no selectivity whatever and should be avoided. By extrapolation, the high-affinity GCaMP6m (K_d 0.16 μM [26]) is also likely to be a poor choice for local Ca^{2+} recordings. At the other end of the spectrum, the lowest affinity reporters (LAR-GECO1.2 and G-GECO1.2-F90L, K_d 12–14 μM) showed the best local selectivity but at the price of a vastly reduced signal amplitude and detection percentage that was, to all intents and purposes, unusable. The sweet-spot optimum was a K_d of ~1 μM . Although O-GECO1 and

RCaMP181 have affinities in this 1 μM range, they were more difficult to use, either because expression was variable or dim, or because signals proved noisier because of the smaller dynamic range. Ultimately, G-GECO1.2 was the best for monitoring lysosomal Ca^{2+} because it had an appropriate K_d , was robustly expressed, bright and has a decent dynamic range.

We also performed additional controls to confirm that a major component of the signals measured by TPC2-G-GECO1.2 derive from Ca^{2+} around the channel and not from Ca^{2+} from other sources. Previously [19] and herein, we show that TPC2-G-GECO1.2 responses persist even after the removal of other Ca^{2+} sources (the ER, or Ca^{2+} influx across the plasma membrane) or by chelating global Ca^{2+} signals with cytosolic EGTA [19]. Complementary to this, ER-mediated Ca^{2+} release (by IP_3 production or SERCA inhibition) failed to generate a TPC2 Ca^{2+} nanodomain [19]. In the current manuscript, we extended the analysis and showed that the large TPC2-G-GECO1.2 response was: (a) not simply due to over-expression of TPC2; (b) not mimicked by targeting the GECI to the lysosome via a different protein, LAMP1; (c) was not due to a bystander detection of Ca^{2+} release from the ER, even with TPC2 overexpression.

Our use of LAMP1-G-GECO1.2 shed additional light on macrophage Ca^{2+} -signalling elements. First, the majority of lysosomes of RAW264.7 cells do not appear to be in close proximity to IP_3 Rs, at least initially; we conclude this because when RAW264.7 cells were stimulated with a pure IP_3 -linked agonist (UTP) the LAMP1-G-GECO1.2 signal was the same magnitude as that of the untargeted soluble G-GECO1.2, indicating that it is only detecting global Ca^{2+} spill over (Fig. 3D,E). This contrasts with HeLa cells where LAMP1-G-GECO1.2 detected larger IP_3 -stimulated Ca^{2+} signals because a substantial proportion (~60%) of lysosomes are in contact sites with ER containing IP_3 Rs [25]. We cannot formally exclude that a small fraction of lysosomes are juxtaposed to the ER in RAW264.7 cells, but only higher spatial resolution recordings might reveal this.

Although LAMP1-G-GECO1.2 was not apposed to IP_3 Rs, we found that it did lie close to adjacent TPC2 (be it endogenous or ectopically expressed) as judged by its detecting larger local Ca^{2+} signals than cytosolic G-GECO1.2 could not (Fig. 3C). We do not necessarily invoke a molecular complex, but it is sufficiently near to detect some of the TPC2 Ca^{2+} nanodomain(s) (Fig. 6F). This functional proximity incidentally provides an explanation for why Ca^{2+} -buffering proteins tethered to lysosomes via LAMP1 were able to *trans*-inhibit TPC2-dependent phagocytosis [19].

3.2. $[Ca^{2+}]$ nanodomain amplitudes

An unsolved issue in the field is the absolute amplitude of local Ca^{2+} nanodomains at TPC2 (or indeed any lysosomal Ca^{2+} channel). The use of different-affinity GECIs allowed us to calibrate the TPC2-G-GECO1.2 signals in terms of absolute $[Ca^{2+}]$ by solving simultaneous equations that have been validated against other calibration approaches [31], and surprisingly revealed that the recorded local change in Ca^{2+} was only

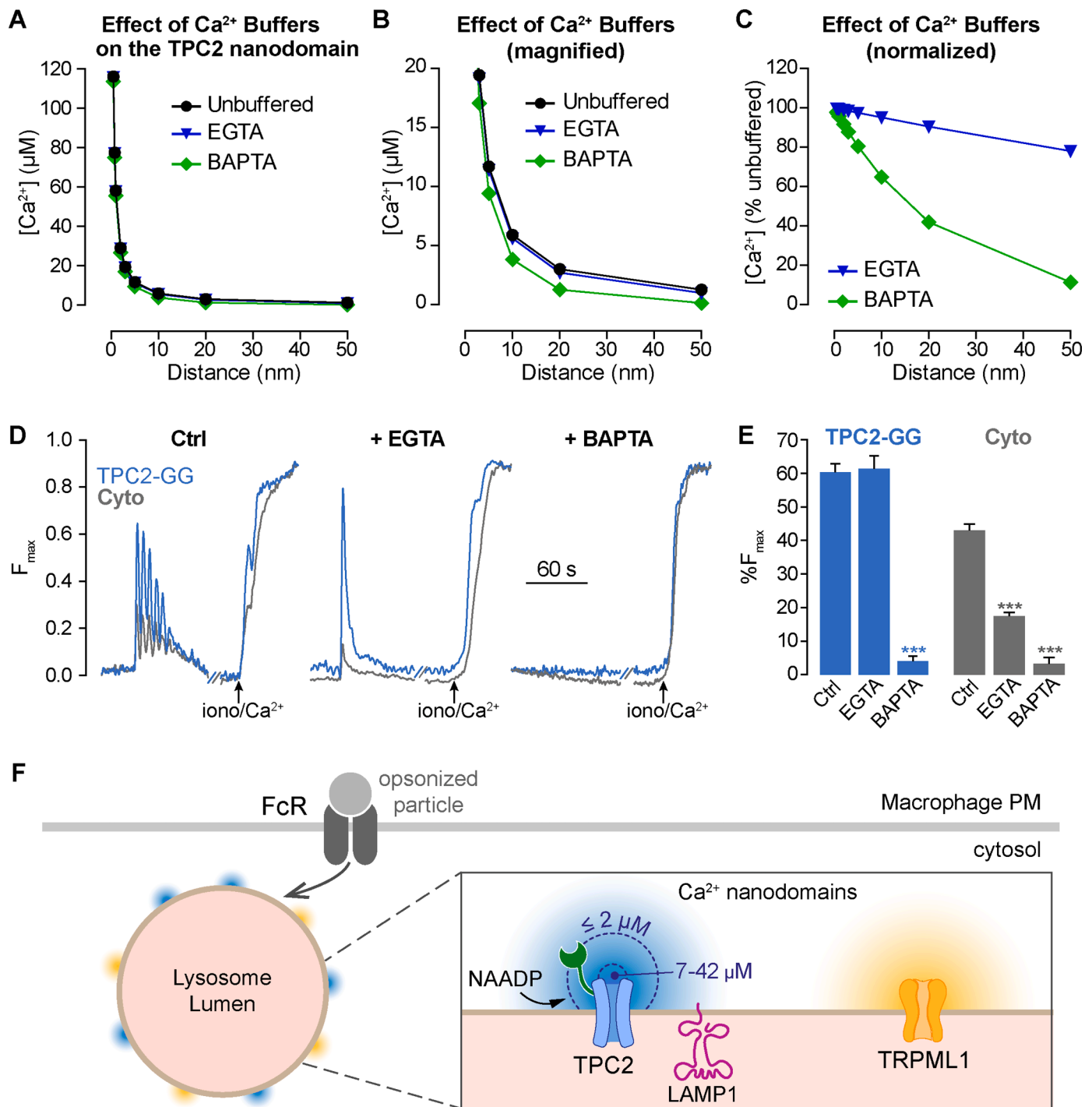


Fig. 6. Effect of slow EGTA and fast BAPTA chelators upon the modelled or measured Ca^{2+} -nanodomains.

(A-C) Theoretical Ca^{2+} -nanodomain profiles in the presence and absence of Ca^{2+} chelators. (A) Effect of EGTA or BAPTA (1 mM each) upon the maximum absolute $[\text{Ca}^{2+}]$ nanodomain using the Neher model. (B) Same data as A, but decreasing the Y-axis limits to magnify the lower $[\text{Ca}^{2+}]$. (C) The $[\text{Ca}^{2+}]$ in the presence of the chelators in A and B normalized to the Unbuffered $[\text{Ca}^{2+}]$ at each respective distance. (D-E) Experimental Ca^{2+} -nanodomains monitored with TPC2-G-GECO1.2 in RAW264.7 cells stimulated with 3- μm beads in the presence and absence of cytosolic EGTA or BAPTA loaded as AM-esters. Global cytosolic $[\text{Ca}^{2+}]$ was simultaneously recorded with Calbryte590 (grey). (E) Collated data from 37 to 60 cells ($N = 5-11$). Significant decreases in signals ($P < 0.001$, ***, ANOVA, Tukey-Kramer post test). (F) Cartoon summary depicting the spatial segregation of the Ca^{2+} nanodomains generated by TPC2 (blue) and TRPML1 (yellow) around the surface of a single lysosome during FcR-mediated phagocytosis. Magnified inset suggests that upon TPC2 activation by cytosolic NAADP, the TPC2 core nanodomain $[\text{Ca}^{2+}]$ is $\leq 42 \mu\text{M}$ at the channel mouth, but the fused-GECI (green) records a $[\text{Ca}^{2+}] \leq 2 \mu\text{M}$ because it is 5–10 nm away from mouth, at the edge of the nanodomain. Whilst the TPC2 and TRPML1 are well separated from one another, the non-channel, LAMP1, lies closer to the TPC2 and is exposed to Ca^{2+} spilling over from the nanodomain.

twice that of the bulk cytosol. The peak local $[Ca^{2+}]$ was only 0.7–2 μM , which partly explains why GECIs with the K_d closest to this range are the best reporters (and intuitively agrees with the 40–50% occupancy of G-GECO1.2 whose K_d is 1.2 μM).

We next wondered why the $[Ca^{2+}]$ at the TPC2 nanodomain might be reported as so low a value, particularly because it would be hard to envisage how lysosomes could entrain their own unique downstream physiological responses when the local Ca^{2+} changes are only two-fold different from the global Ca^{2+} . We suggest that this can be reconciled if the tethered GECIs are physically placed at the *edge* (and not the core) of the channel Ca^{2+} nanodomain. From our structural modelling, the closest average distance that the GECI might be is ~ 5 nm whereas in an extended conformation it was ~ 10 nm, and the Ca^{2+} gradient falls off steeply over this scale [2,32,33]. Such scaling of the Ca^{2+} nanodomain is also consistent with the effects of EGTA and BAPTA: in macrophages, TPC2-dependent Ca^{2+} signalling is blocked by fast BAPTA but not slow EGTA [19] whose spatial ranges of action are around 7–10 nm and 136–300 nm respectively [2,39]. This is also reflected in the differential effects of these chelators on the TPC2 nanodomain profile, both theoretically (Fig. 6A–C) and experimentally (Fig. 6D,E) when assessed with TPC2-G-GECO1.2 (see Methods and Fig. S4G,H).

We acknowledge that we cannot be overly dogmatic about our extrapolated estimates for the true nanodomain $[Ca^{2+}]$ because there are several unknowns such as the characteristics of the cytosolic Ca^{2+} -buffering/ Ca^{2+} -diffusion and, crucially, the absolute conformation of the C-terminus of TPC2-G-GECO1.2 (e.g. the GECI might be even further away from the pore than 10 nm which would increase the maximum calculated core $[Ca^{2+}]$ calculation, see Fig. 5I). Ca^{2+} -nanodomain modelling argues that Ca^{2+} buffering is unlikely to greatly impact our estimates: the core of the Ca^{2+} nanodomain is little affected by local immobile buffers [32] or by endogenous mobile buffers which only alter the core Ca^{2+} nanodomain by $\sim 1\%$ (Fig. S4D–F). Although buffering might reduce the $[Ca^{2+}]$ 5–10 nm away (e.g. 1 mM endogenous mobile buffers reduce this distal $[Ca^{2+}]$ by only 10–20%, Fig. S4D–F), this equates to the GECI underestimating the core $[Ca^{2+}]$ nanodomain by only 1%.

In contrast to the minor influence of endogenous buffering, the pore-GECI distance has a profound impact upon the estimates of the nanodomain $[Ca^{2+}]$ and is a credible explanation for the relatively low $[Ca^{2+}]$ values reported by the GECI. Our data point to the true TPC2 Ca^{2+} nanodomain being somewhere between 7 and 21 μM and 14–42 μM , a selectivity of some 14- to 84-fold over the peak global cytosolic $[Ca^{2+}]$ (~ 0.5 μM). Of the two bands, we favour the higher 14–42 μM for several reasons: (a) sterically, it is unlikely that at any given time that both copies of G-GECO1.2 are crammed into the narrow confines of the TPC2 dimer ‘funnel’ (i.e., the minimum ‘compact’ distance, Fig. 5D,F); (b) the surface charges of the G-GECO1.2 are substantially negative and inter-molecular repulsion will make their close association in the funnel even less favourable (Fig. 5E). The band of higher values, plus its BAPTA-susceptibility (Fig. 6, Fig. S4G,H), would agree with the categorization of the TPC2 local $[Ca^{2+}]$ as a nanodomain rather than a microdomain [38].

Our modelling of the theoretical Ca^{2+} -nanodomain profile used the single-channel current adjusted for the open probability (P_o) of the channel. Note that the relative (normalized) shape of the Ca^{2+} -nanodomain profile is completely independent of the absolute current values that are chosen, the $[Ca^{2+}]$ values are simply scaled up or down accordingly, and so our GECI distance-corrections are unaffected by errors in the absolute current used. The P_o -adjusted single-channel current is appropriate because we have monitored single-cell Ca^{2+} nanodomain changes over a timescale of seconds and have determined the peak $[Ca^{2+}]$ which is an ensemble average of many TPC2 channels across numerous lysosomes. The lysosomal luminal pH in RAW264.7 cells is 4.7–4.9 [40,41] and, at pH 4.8, the P_o of TPC2 channels varies as a function of the NAADP concentration as a bell-shaped curve, and a maximum P_o of ~ 0.015 [37]. Using this P_o , the maximum theoretical

nanodomain $[Ca^{2+}]$ close to the pore would be 116 μM (Fig. 5G). From our empirical estimate of the $[Ca^{2+}]$ as being 14–42 μM we could estimate that the P_o during physiological stimulation is likely to reflect, on average, sub-maximal channel activation and, indeed, a P_o closer to 0.005 more faithfully recapitulates the nanodomain core- and edge- $[Ca^{2+}]$ values that we have calculated (Fig. S4C). However, without the determination of the organellar TPC2 single-channel recordings in intact cells, which is technically impossible, we can only offer this as a speculative guide.

Given a Ca^{2+} nanodomain of 14–42 μM , this is a system in which closely apposed low-affinity Ca^{2+} -binding proteins becomes a viable framework for the selective decoding of lysosomal Ca^{2+} signals [42]. In macrophages, we proposed recently that the TPC Ca^{2+} nanodomains are decoded by the Ca^{2+} -dependent phosphatase, calcineurin (CN) which, in turn, dephosphorylates and activates dynamin, the GTPase essential for phagocytosis [19]. Full activation of CN requires Ca^{2+} binding at both high- (0.024–0.9 μM) and low-affinity (15–37 μM) sites [5]. Since the maximal global Ca^{2+} signals upon FcR engagement are only 0.2–0.5 μM (Fig. 5A,B), CN is unlikely to be fully activated by global cytosolic Ca^{2+} ; conversely, our estimates of the TPC2 Ca^{2+} nanodomain are in good agreement with the CN low-affinity site and thereby provide a tempting explanation for why TPCs uniquely drive Ca^{2+} -dependent phagocytosis [19].

For context, local Ca^{2+} concentrations around other Ca^{2+} channels are Orai-1 (1.4 μM) [43], L-type Ca^{2+} channels (20–25 μM) [44], IP₃Rs (5–50 μM) [45–48], which broadly correlates with their single-channel conductances (the local $[Ca^{2+}]$ is proportional to the single-channel Ca^{2+} conductance [32] (Fig. S4C)): Orai1 (0.007–0.8 pS [Orai-1] [49]; L-type VGCC (2.4 pS) [50], IP₃Rs (12–53 pS) [48,51]. Considering that the TPC2 unitary Ca^{2+} conductance is 15–40 pS [27,37], our distance-adjusted estimate for the TPC2 Ca^{2+} nanodomain is in line with what one might expect. Note, however, that TPC2 conductances were not determined in situ (in the lysosome), and their improper location (lipid bilayers, plasma membrane), channel truncation and non-physiological pH may affect the Ca^{2+} conductances. Our in situ determinations of the Ca^{2+} nanodomain do have an advantage in that regard.

In summary, the reason why GECIs with a $K_d \sim 1$ μM are optimal is because this matches the $[Ca^{2+}]$ at the edge of the Ca^{2+} nanodomain where the GECIs are placed in space. A distance-adjusted estimate of the true core of the Ca^{2+} nanodomain is up to 84-fold greater than the cytosol and consistent with the value of other channels.

3.3. Different Ca^{2+} channels evoke independent Ca^{2+} nanodomains

FcR-dependent phagocytosis activates multiple Ca^{2+} -channel families simultaneously, but whether Ca^{2+} is actually important for particle uptake has been much debated (reviewed [18]). We argue that the controversy can be partly resolved by recognizing that lysosomal Ca^{2+} stores are a major contributor to phagocytosis, at least in mouse macrophages, with TPCs being a universal requirement for a range of particle sizes and shapes [19] whereas TRPML1 is additionally recruited for large-particle phagocytosis [19,20]. TPCs appear to couple to the activation of dynamin, which plays multiple roles at phagocytosis including scission of the nascent phagosome and actin rearrangement [5,52,53]. Playing a more specialist role, TRPML1 promotes lysosomal exocytosis, so that vesicle fusion with the plasma membrane provides the additional membrane necessary to coat large particles being phagocytosed [19,20]. Currently, the best evidence suggests that, at phagocytosis, TPCs are stimulated by the soluble second messenger, NAADP [19], whereas TRPML1 is stimulated by PI(3,5)P₂ [20] (whether PI(3,5)P₂ also contributes to TPC2 activation at phagocytosis is currently unknown). At phagocytosis, Ca^{2+} -binding decoding proteins that have been implicated are calcineurin for TPCs [19] and synaptotagmin-VII for TRPML1 [20,54].

Importantly, TPC channels cannot be substituted for by other Ca^{2+}

channels: the phagocytic deficiency in TPC-knockout macrophages cannot be rescued by IP₃Rs or TRPML1 activation [19], proving that TPCs generate a functionally unique Ca²⁺ signature. In other systems, lysosomal Ca²⁺ is selective over ER-derived Ca²⁺ in regulating processes such as neurite outgrowth [55], muscle differentiation [56] and blood pressure [57], but the side-by-side comparison of the different roles of TPCs and TRPMLs in the same cell type are fewer in number, in spite of the universal expression of these channels. Examples include TRPML1 (but not TPC2) regulating TFEB translocation [7] or lysosomal size [8]. Conversely, TPC2 (but not TRPML1) is the predominant drive of choroidal angiogenesis [9], macropinosome resorption [10] and oxytocin neurosecretion [11].

If different downstream pathways are recruited by different channels, this implies that the downstream Ca²⁺-decoders are only activated by the Ca²⁺ nanodomain of the source channel, and not by more distal ones. As discussed above, the most likely architecture is for each low-affinity Ca²⁺-decoder to be closely apposed to its cognate channel and uniquely activated by the proximal Ca²⁺ nanodomain [2]. But what occurs when multiple Ca²⁺-channel types are present in the same membrane? Pairs of adjacent Ca²⁺-channel families manifestly act independently from one another in a non-redundant manner, whether at the plasma membrane (TRPV1 and P2X4 [58] or Orai and TRPC3 [59]) or the ER (IP₃Rs and RyRs [60,61]). But the surface area of a lysosome is smaller and more restricted than that of the ER or plasma membrane (assuming spheres of 0.5, 5 and 20 µm diameters respectively, the areas of the ER and plasma membrane are 100- and 1600-fold larger than a lysosome). It was therefore important to verify that, in the confined lysosomal membrane, the Ca²⁺ channels evoked Ca²⁺ signals that did not spill over onto one another and potentially cross-activate the Ca²⁺-decoder(s) of the other family. We therefore activated each (primary) channel family and tested whether the complementary (secondary) family could passively detect Ca²⁺ signals spilling over.

By fusing the GECI to the non-activated channel of the pair, we could determine whether Ca²⁺ passively spilled over between TPC2 and TRPML1. Consequently, when cells were stimulated by small (3-µm) beads to uniquely activate TPC2, adjacent TRPML1-G-GECO1.2 only detected the global (cytosolic) spill-over and not any lysosomal spill over. This was not because endogenous TPC2 Ca²⁺ nanodomains are too small to detect with the G-GECO1.2 because the LAMP1-G-GECO1.2 version was indeed able to record endogenous local lysosomal domains, presumably because of greater proximity to TPC2. Conversely, cells stimulated with large (6-µm) beads to activate endogenous TRPML1 showed only a minor spill-over onto pore-dead TPC2-D276K-G-GECO1.2 (an inactive surrogate for TPC2) which predominantly recorded the usual component emanating from the global cytosol. Given that the G-GECO1.2 Ca²⁺ affinity is 1.2 µM, then the maximum spill over from TRPML1 to TPC2-D276K-G-GECO1.2 was observed with ~23% occupancy of the G-GECO1.2 in these experiments (cf. cytosolic G-GECO1.2 of ~12% in parallel). Using the standard intensimetric reporter calibration equation of Grynkiewicz et al. [62], we can approximate that the TPC2 is sensing a local [Ca²⁺] spill-over of ~350 nM. If the core of the self-generated TPC2 Ca²⁺ nanodomain is 7–42 µM, then this spill-over from TRPML1 is merely 1–11% of that, and therefore unlikely to be of functional significance.

All in all, the data provide a potential explanation for why TPC2 does not drive lysosomal exocytosis at phagocytosis because the Ca²⁺ it releases would not reach the exocytotic machinery that is presumably adjacent to TRPML1 [20]. This is also consistent with the fact that when an NAADP mimetic is used to stimulate TPC2 channels in macrophages it fails to support lysosomal exocytosis [21]. The spatial segregation of the two channel families is likely to be architecturally feasible even at the level of a single vesicle. Assuming the diameter of a lysosome is 0.5–2.0 µm and that of each channel oligomer is ~8 nm, we previously calculated that even 500 channels would only occupy 0.4–6.4% of the lysosome surface area [19], when others have estimated that there might be only 20 TPC2 channels per lysosome endogenously [63]. Therefore,

there is more than ample space to keep the channel families apart. We therefore propose a model whereby Ca²⁺ that is released from lysosomal Ca²⁺ channels does not generate a contiguous ‘halo’ of high [Ca²⁺] around the lysosome but rather a discontinuous ‘mosaic’ of Ca²⁺ nanodomains associated with each channel point-source (Fig. 6F).

Although there are a few reports directly comparing the physiological roles of these lysosomal channel families showing either an exclusive coupling of TPC2 [9,19] or TRPML1 [7,8], a demonstration of their separate Ca²⁺ domains had not been confirmed previously. Electrophysiologically, TRPML1 and TPC2 behave as independent channels, even when over-expressed [64], and our *in situ* optical recordings affirm that.

4. Conclusion

By defining the GECI properties important for selective lysosome Ca²⁺ channel recordings, we have rigorously characterized the amplitude and spread of lysosomal Ca²⁺ nanodomains. We have further revealed that families of lysosomal Ca²⁺-channels act in a largely autonomous manner to generate their own unique Ca²⁺ nanodomains that do not cross-contaminate one another. Determining Ca²⁺ fluxes optically *in situ* has the advantage over electrophysiology in being an intact-cell approach that does not require the swelling of lysosomes as a result of the perturbation of lysosomal lipids [65]. Although we have used a physiological macrophage phagocytosis model, our results will have wider impact across biology where the unique role of lysosomal Ca²⁺ stores is growing in importance for pathologies including cancer [16] and neurodegeneration [66] but, until now, how lysosomal Ca²⁺ signals were compartmentalized was poorly understood. From here on in, we should be able to better understand how lysosomal Ca²⁺ signals are generated, separated and decoded by proteins with appropriate Ca²⁺ affinities.

5. Material and methods

5.1. Cell culture and transfection

RAW264.7 murine macrophages were cultured in DMEM supplemented with 10% v/v FCS, 2 mM glutamine, 100 U/ml penicillin and 100 µg/ml streptomycin, at 37 °C under 5% CO₂. RAW264.7 were transfected using JetPRIME (Polyplus transfection), in ratios of 1 µg of endotoxin-free plasmid DNA with 2 µl of JetPRIME, and incubated for 24 h before analysis.

5.2. Plasmids

GECIs were fused to the C-terminus of human TPC2 (BC063008) and were generated in-house using restriction cloning or Gibson cloning (NEBuilder High Fidelity): the human versions of TPC2-G-GECO1.2, TPC2-D276K-G-GECO1.2 and TRPML1-G-GECO1.2-ERES (with an ER-Export Signal) were described in [19]. GCaMP3 and RCaMP181 were kind gifts from Sandip Patel (University College London) and Loren Looger (University of California, San Diego) respectively; GCaMP6s, O-GECO1 and LAR-GECO1.2 were obtained from Addgene: pGP-CMV-GCaMP6s was a gift from Douglas Kim & GENIE Project (Addgene plasmid # 40,753; <http://n2t.net/addgene:40753>; [26]), CMV-O-GECO1 was a gift from Robert Campbell (Addgene plasmid # 46,025; <http://n2t.net/addgene:46025>; [67]), CMV-mito-LAR-GECO1.2 was a gift from Robert Campbell (Addgene plasmid # 61,245; <http://n2t.net/addgene:61245>; [68]). Mutants of G-GECO1.2 were constructed by site-directed mutagenesis and confirmed by sequencing. LAMP1-mGFP was a kind gift Dr Esteban Dell’Angelica (University of California, USA) [69] and used as a template for the mCherry version.

5.3. Opsonized beads

50 mg carboxylated, 3- μ m diameter, silica beads (Kisker Biotech) were incubated with 50 mg/ml cyanamide in PBS pH 7.2 for 15 min. Excess cyanamide was removed by washing in 0.1 M sodium borate, pH 8. Fatty acid-free BSA (10 mg) and mouse IgG (1 mg) in 0.1 M sodium borate, pH 8 were added to the beads and incubated with agitation for 4 h. The beads were washed in 250 mM glycine in PBS pH 7.2, followed by PBS pH 7.2, and stored at 4 °C in PBS. For 6- μ m silica beads (Polysciences Europe GmbH), a similar procedure was followed except that the mouse IgG was increased to 5 mg to compensate for the larger surface area.

5.4. Intracellular Ca^{2+} measurements

RAW264.7 cells were loaded with 2 μ M Calbryte 520/AM or 2 μ M Calbryte 590/AM in the presence of 0.03% w/v Pluronic F-127 in extracellular medium (ECM, mM: 121 NaCl, 5.4 KCl, 0.8 $MgCl_2$, 1.8 $CaCl_2$, 6 $NaHCO_3$, 25 HEPES, 10 Glucose) supplemented with essential amino acids, for 45–60 min at room temperature, followed by a 15 min de-esterification. Alternatively, cells were transfected with plasmids to express cytosolic GECIs or TPC2-tethered GECIs. For experiments conducted in Ca^{2+} -free medium, cells were washed once with Ca^{2+} -free ECM supplemented with 1 mM EGTA, followed by two washes in Ca^{2+} -free ECM plus 100 μ M EGTA and experiments conducted in this same medium.

RAW264.7 expressing GECIs with or without co-loading with orthogonal Calbryte 520/590 were imaged using a Nikon A1R laser-scanning confocal equipped with a Plan Apo VC 20 \times DIC N2 objective in resonant-scanner mode, with an image collected every 0.533 s. In Channel-Series mode, green and red fluorophores were alternately excited at 488 and 561 nm, and emission was centred at 525 and 595 nm, respectively. Experiments were conducted on a heated stage at approx. 34 °C.

5.5. Protein modelling

To generate structures of previously undetermined protein sequences, we used ColabFold (monomeric or multimeric modelling) [35] hosted by the University of Oxford's ARC (Advanced Research Computing) facility to generate 10 models per sequence. Of these, we used the highest ranked, relaxed models to generate images, manipulate structures and quantify distances within the Chimera X software (version 1.4) [70]. Models and empirical structures were compared and overlapped using an unbiased fitting function (Matchmaker), except when we constrained the fit of the CaM domain (147 residues) of G-GECO1.2 to the CaM of R-GECO1. The difference between the model and empirical structures was quantified as the root mean square deviation (RMSD) in Å. The *Join Models* routine produced TPC2-G-GECO1.2 fusion proteins from the separate Colabfold-generated PDB files of the full-length human TPC2 and linker-G-GECO1.2 (varying the connecting ω - and ϕ -bond torsion angles between -180 to +180, and -120 to +120° respectively). For the minimum-distance model, we manually aligned two copies of the unfused linker-G-GECO1.2 'head-to-head' within the TPC2 'funnel' in the same program. Reference structures were human TPC2 (PDB: 6NQ0) [34] and Ca^{2+} -bound R-GECO1 (PDB: 4I2Y) [71].

5.6. Data analysis

Amplitudes and kinetics of single-cell fluorescence changes were analysed using custom-written software (Magipix, Dr Ron Jacob, King's College London). Recordings were normalized to each single cell's maximum fluorescence determined by 1 μ M ionomycin plus 10 mM Ca^{2+} added at the end of the run and expressed as a percentage of this maximum i.e., $100 \times (F - F_0)/(F_{max} - F_0)$, where F is the fluorescence at any time, F_0 is the average initial fluorescence and F_{max} is that determined

upon ionomycin/ Ca^{2+} . This is abbreviated on graph axes to '% F_{max} '. For clarity, in Fig. 4, we subtracted the mean cytosolic G-GECO1.2 peak responses from each single-cell channel-G-GECO1.2 fusion peak response to give 'channel – cytosol' changes.

5.7. Pair-wise calibration of Ca^{2+} nanodomains

To convert fluorescence signals into absolute $[Ca^{2+}]$, we adopted the approach of [31]. In brief, since the same Ca^{2+} response was monitored with different GECIs, the two unknowns (resting and stimulated $[Ca^{2+}]$) can be determined by simultaneous equations for a pair of GECIs, solved numerically by the Newton-Raphson method. For each GECI, the Ca^{2+} response is defined by this equation:

$$\frac{F_s}{F_r} = \frac{1 + (R_f - 1) \frac{[Ca^{2+}]_s^{n_H}}{K_d + [Ca^{2+}]_s^{n_H}}}{1 + (R_f - 1) \frac{[Ca^{2+}]_r^{n_H}}{K_d + [Ca^{2+}]_r^{n_H}}}$$

F_s and F_r are the stimulated peak and resting fluorescences respectively; R_f is the dynamic range of the reporter (defined as the known ratio of F_{max}/F_{min}); K_d is the dissociation constant of the GECI (in micromolar); $[Ca^{2+}]^{n_H}$ is the absolute Ca^{2+} concentration (micromolar) raised to the exponent of the Hill Slope (n_H), with the subscripts 's' and 'r' denoting the stimulated and resting values respectively [31]. The values of the K_d , dynamic range and Hill slope were taken from Table 1 (for the published GECI), an average being used when multiple values are reported, or using our own experimentally determined K_d and n_H for the G-GECO1.2 mutants. For the F_s/F_r ratio, we used the mean F/F_0 value across all experiments.

The simultaneous equations for each GECI pair were solved using the routine available at <https://github.com/jaimedejuan/pair-wise-indicator-calcium> and run under Mathematica 12 (Wolfson). All permutations of the different GECIs pairs were solved for the resting and stimulated $[Ca^{2+}]$ and collated as the mean \pm SEM. For example, 6 GECIs produce 15 paired sets of resting and stimulated $[Ca^{2+}]$.

5.8. Ca^{2+} -nanodomain modelling

To model the Ca^{2+} -domain spatial profile, we applied the equation of Neher that describes the unbuffered spatial profile of a Ca^{2+} domain [2, 36,72]:

$$[Ca^{2+}]_{Nano} = \frac{\phi}{4\pi r D_{Ca}} + [Ca^{2+}]_o$$

Where $[Ca^{2+}]_{Nano}$ is the $[Ca^{2+}]$ in the local domain, $[Ca^{2+}]_o$ is the basal $[Ca^{2+}]$, ϕ is the TPC2 single-channel Ca^{2+} flux (in mol/s), r is the distance from the mouth of the pore, D_{Ca} is the diffusion coefficient of free Ca^{2+} (230 $\mu m^2/s$ [73]). Since the TPC2 single-channel Ca^{2+} current (I) has not been reported, this was calculated from the single-channel properties of human full-length TPC2 [37]: single-channel Ca^{2+} current was derived from the single-channel conductance (g , 15 pS) using $I = gE$, where the driving force $E = V_{Lys} - E_{Ca}$ (V_{Lys} = lysosomal membrane potential; E_{Ca} = the equilibrium potential for Ca^{2+} assuming the $[Ca^{2+}]$ in the lumen and cytosol is 0.5 mM and 100 nM respectively i.e. an E_{Ca} of +114 mV, and a lysosomal membrane potential of -30 mV (reported ranges of -19 to -100 mV [40,74,75]) to give a current of 2.16 pA. We adjusted this for the open probability (P_o) of TPC2, which varies with the NAADP concentration and is maximally 0.015 at an appropriately acidic luminal pH of 4.8 [37]; this gives the maximal single-channel TPC2 current as being 0.032 pA. Using divalent Ca^{2+} flux = $I/2F$ (where $F = 9.65 \times 10^4$ C/mol), the TPC2 single-channel Ca^{2+} flux was determined as 1.68×10^{-19} mol/s. To assess the effect of P_o on the nanodomain $[Ca^{2+}]$, analogous calculations were performed using a range of P_o values from 0.001 to 0.5 (Fig.S4A-C).

We used the unbuffered model because the Ca^{2+} buffering around lysosomal channels is unknown. It should be noted that extending the

model to include Ca^{2+} buffers [32] had only subtle effects upon the nanodomain spatial profile over these distances, with little effect upon the core Ca^{2+} nanodomain itself (see Fig. S4D-F). For this, we used a modification of the equation above [32]:

$$[\text{Ca}^{2+}]_{\text{Nano}} = \frac{\phi}{4\pi r D_{\text{Ca}}} e^{-\lambda r} + [\text{Ca}^{2+}]_0$$

Definitions as above except $\lambda = \sqrt{(D_{\text{Ca}}/(k_{\text{B}}[\text{B}]))}$, where k_{B} is the rate constant of Ca^{2+} binding to the buffer, and $[\text{B}]$ is the concentration of the buffer. k_{B} ($\text{M}^{-1} \text{s}^{-1}$) values for buffers were EGTA (2.5×10^6), BAPTA (4×10^8) and endogenous mobile buffer (1×10^8) [32].

5.9. Determination of the Ca^{2+} affinity of G-GECO1.2 mutants

Recombinant GECI proteins were purified from bacteria and their fluorescence monitored in a plate-reader with solutions clamped at different $[\text{Ca}^{2+}]$. First, mutant G-GECO1.2 sequences were cloned into a pET16b bacterial expression vector downstream of OmpA and His₆-tag sequences. OmpA drove secretion of the proteins into the medium, and the His₆-tag used for purification. BL21-CodonPlus (DE3)-RIL bacteria were transformed, and an overnight culture used to inoculate Terrific Broth until an $\text{OD}_{600 \text{ nm}}$ 0.45 was reached at 37 °C. Protein expression was then induced with 0.5 mM IPTG for 22 h at room temperature with shaking at 200 rpm. Following centrifugation at 10k g for 10 min at 4 °C, the culture medium containing the secreted His₆-G-GECO1.2 protein was supplemented with 300 mM NaCl, 50 mM HEPES pH 7.5 and Complete™ EDTA-free protease inhibitor cocktail (Roche). Protein was purified on HisPur cobalt resin (ThermoFisher Scientific) for 1 h at 22 °C. The resin was washed 5x with 50 mM sodium phosphate buffer pH 7.7, 300 mM NaCl, 25 mM imidazole, 0.03% Triton x-100, and purified protein eluted in 50 mM sodium phosphate buffer pH 7.7, 300 mM NaCl, 300 mM imidazole. Proteins were dialysed in a 10k MWCO Slide-A-Lyzer dialysis cassette (ThermoFisher Scientific) against 20 mM Tris pH 8.0 and 100 mM NaCl, overnight at 4 °C. Finally, the protein was concentrated using 10k MWCO Amicon Ultra-0.5 centrifugal filter devices. Purification was confirmed by SDS-PAGE and proteins detected using Imperial Protein Stain (ThermoFisher Scientific).

In a 96-well plate, fluorescence was monitored of a 1:100 dilution of G-GECO1.2 variants in an intracellular-like medium (ICM, mM: 140 KCl, 10 NaCl, 14 HEPES acid, 6 HEPES salt, pH 7.2) containing different Ca^{2+} /chelator ratios that gave different free $[\text{Ca}^{2+}]$ (from nM to mM). $\text{Ex} = 473 \text{ nm}$, $\text{Em} = 557 \text{ nm}$. Stock solutions of 100 mM chelator \pm 100 mM Ca^{2+} (pH 7.2) were prepared, the Ca^{2+} equivalence of the latter being accurately determined using a pH-metric approach [76]. Each stock was diluted into ICM to give 5 mM of chelator \pm 5 mM Ca^{2+} , and these two solutions were mixed in different ratios to give different free $[\text{Ca}^{2+}]$ determined by Winmaxchelator (C. Patton, Stanford, USA). To cover a range of $[\text{Ca}^{2+}]$, we used the chelators EGTA, HEDTA and NTA (nitrilotriacetic acid) (all from Merck Life Science), 5,5'-Dibromo-BAPTA (Insight Biotech. Ltd.). Fluorescence was normalized to the minimum and maximum values per GECI, and data fitted by Graphpad Prism 6 using a single binding site (variable Hill slope).

5.10. Statistical analysis

Statistics were determined either using Graphpad Prism 6 or Graphpad Instat 3.1. Two data sets were compared using Student's *t*-test, whereas a one-way ANOVA and Tukey-Kramer (or Bonferroni) post-hoc test were used for 3 or more conditions. Data were paired where appropriate. Normality was determined the Kolmogorov and Smirnov test, and non-parametric tests applied when data failed normality. Experiments were conducted on at least 3 separate cell preparations on different days, with multiple transfection-replicates per condition. Data throughout are expressed as the mean \pm S.E.M. of *n* cells from *N* different experiments.

CRedit authorship contribution statement

Lianne C. Davis: Conceptualization, Methodology, Formal analysis, Investigation, Writing – review & editing, Visualization. **Anthony J. Morgan:** Conceptualization, Methodology, Formal analysis, Investigation, Writing – original draft, Writing – review & editing, Visualization, Funding acquisition. **Antony Galione:** Conceptualization, Writing – review & editing, Funding acquisition.

Declaration of Competing Interest

The authors declare no conflict of interest.

Data availability

No data was used for the research described in the article.

Acknowledgements

We would like to thank Dr Alexander Grassam-Rowe (this department) for assistance in setting up the ColabFold interface hosted by the University of Oxford's Advanced Research Computing (ARC) facility, whom we gratefully acknowledge, <https://doi.org/10.5281/zenodo.225558>. We also thank Dr Paolo Tammaro (this department) for invaluable discussions surrounding single-channel conductances. The work was funded by a BBSRC grant to AJM and AG (BB/T01640X/1) and a Wellcome Trust Senior Investigator Award to AG (102828/Z/13/Z).

Supplementary materials

Supplementary material associated with this article can be found, in the online version, at [doi:10.1016/j.ceca.2023.102801](https://doi.org/10.1016/j.ceca.2023.102801).

References

- [1] M.J. Berridge, The inositol trisphosphate/calcium signaling pathway in health and disease, *Physiol. Rev.* 96 (2016) 1261–1296.
- [2] A.B. Parekh, Ca^{2+} microdomains near plasma membrane Ca^{2+} channels: impact on cell function, *J. Physiol. (Lond.)* 586 (2008) 3043–3054.
- [3] P. Li, M. Gu, H. Xu, Lysosomal ion channels as decoders of cellular signals, *Trends Biochem. Sci.* 44 (2) (2019) 110–124.
- [4] J. Xiong, M.X. Zhu, Regulation of lysosomal ion homeostasis by channels and transporters, *Sci. China Life Sci.* 59 (2016) 777–791.
- [5] A.J. Morgan, L.C. Davis, A. Galione, Choreographing endo-lysosomal Ca^{2+} throughout the life of a phagosome, *Biochim. Biophys. Acta Mol. Cell Res.* 1868 (2021), 119040.
- [6] S. Patel, Y. Yuan, C.C. Chen, D. Jaslan, G. Gunaratne, C. Grimm, T. Rahman, J. S. Marchant, Electrophysiology of endolysosomal two-pore channels: a current account, *Cells* 11 (15) (2022) 2368.
- [7] D.L. Medina, S. Di Paola, I. Peluso, A. Armani, D. De Stefani, R. Venditti, S. Montefusco, A. Scotto-Rosato, C. Prezioso, A. Forrester, C. Settembre, W. Wang, Q. Gao, H. Xu, M. Sandri, R. Rizzuto, M.A. De Matteis, A. Ballabio, Lysosomal calcium signalling regulates autophagy through calcineurin and TFEB, *Nat. Cell Biol.* 17 (2015) 288–299.
- [8] Q. Cao, Y. Yang, X.Z. Zhong, X.P. Dong, The lysosomal Ca^{2+} release channel TRPML1 regulates lysosome size by activating calmodulin, *J. Biol. Chem.* 292 (2017) 8424–8435.
- [9] Y. Li, C. Schon, C.C. Chen, Z. Yang, R. Liegl, E. Murenu, B. Schworm, N. Klugbauer, C. Grimm, C. Wahl-Schott, S. Michalakakis, M. Biel, TPC2 promotes choroidal angiogenesis and inflammation in a mouse model of neovascular age-related macular degeneration, *Life Sci. Alliance* 4 (8) (2021), e202101047.
- [10] S.A. Freeman, S. Uderhardt, A. Saric, R.F. Collins, C.M. Buckley, S. Mylvaganam, P. Boroumand, J. Plumb, R.N. Germain, D. Ren, S. Grinstein, Lipid-gated monovalent ion fluxes regulate endocytic traffic and support immune surveillance, *Science* 367 (2020) 301–305.
- [11] L.L. Martucci, J.M. Launay, N. Kawakami, C. Sicard, N. Desvignes, M. Dakouane-Giudicelli, B. Spix, M. Tetu, F.O. Gilmaire, S. Paulcan, J. Callebort, C. Vailland, F. Bracher, C. Grimm, P. Fossier, S. de la Porte, H. Sakamoto, J. Morris, A. Galione, S. Granon, J.M. Cancela, Endolysosomal TPCs regulate social behavior by controlling oxytocin secretion, *Proc. Natl. Acad. Sci. U.S.A.* 120 (2023), e2213682120.
- [12] A.J. Morgan, Ca^{2+} dialogue between acidic vesicles and ER, *Biochem. Soc. Trans.* 44 (2016) 546–553.

- [13] P.M. Heister, T. Powell, A. Galione, Glucose and NAADP trigger elementary intracellular beta-cell Ca^{2+} signals, *Sci. Rep.* 11 (2021) 10714.
- [14] Y. Yuan, D. Jaslan, T. Rahman, S.R. Bolsover, V. Arige, L.E. Wagner, C. Abrahamian, R. Tang, M. Keller, A.S. Rosato, E.M. Weiden, F. Bracher, D.I. Yule, C. Grimm, S. Patel, Segregated cation flux by TPC2 biases Ca^{2+} signaling through lysosomes, *Nat. Commun.* 13 (2022) 4481.
- [15] S. Patel, B.S. Kilpatrick, Two-pore channels and disease, *Biochim. Biophys. Acta Mol. Cell Res.* 1865 (2018) 1678–1686.
- [16] C.C. Chen, E. Krogsaeter, C.Y. Kuo, M.C. Huang, S.Y. Chang, M. Biel, Endolysosomal cation channels point the way towards precision medicine of cancer and infectious diseases, *Biomed. Pharmacother.* 148 (2022), 112751.
- [17] M. Xu, X.P. Dong, Endolysosomal TRPMLs in Cancer, *Biomolecules* 11 (1) (2021) 65.
- [18] J. Westman, S. Grinstein, M.E. Maxson, Revisiting the role of calcium in phagosome formation and maturation, *J. Leukoc. Biol.* 106 (2019) 837–851.
- [19] L.C. Davis, A.J. Morgan, A. Galione, NAADP-regulated two-pore channels drive phagocytosis through endo-lysosomal Ca^{2+} nanodomains, calcineurin and dynamin, *EMBO J.* 39 (2020), e104058.
- [20] M. Samie, X. Wang, X. Zhang, A. Goschka, X. Li, X. Cheng, E. Gregg, M. Azar, Y. Zhuo, A.G. Garrity, Q. Gao, S. Slaughterhaupt, J. Pickel, S.N. Zolov, L.S. Weisman, G.M. Lenk, S. Titus, M. Bryant-Genevieve, N. Southall, M. Juan, M. Ferrer, H. Xu, A TRP channel in the lysosome regulates large particle phagocytosis via focal exocytosis, *Dev. Cell* 26 (2013) 511–524.
- [21] S. Gerndt, C.C. Chen, Y.K. Chao, Y. Yuan, S. Burgstaller, A. Scotto Rosato, E. Krogsaeter, N. Urban, K. Jacob, O.N.P. Nguyen, M.T. Miller, M. Keller, A. M. Vollmar, T. Gudermann, S. Zierler, J. Schredelseker, M. Schaefer, M. Biel, R. Malli, C. Wahl-Schott, F. Bracher, S. Patel, C. Grimm, Agonist-mediated switching of ion selectivity in TPC2 differentially promotes lysosomal function, *Elife* 9 (2020) e54712.
- [22] A.L. Ambrosio, J.A. Boyle, S.M. Di Pietro, TPC2 mediates new mechanisms of platelet dense granule membrane dynamics through regulation of Ca^{2+} release, *Mol. Biol. Cell* 26 (2015) 3263–3274.
- [23] O.A. Ogunbayo, J. Duan, J. Xiong, Q. Wang, X. Feng, J. Ma, M.X. Zhu, A.M. Evans, mTORC1 controls lysosomal Ca^{2+} release through the two-pore channel TPC2, *Sci. Signal.* 11 (2018) eaao5775.
- [24] X. Zhang, X. Cheng, L. Yu, J. Yang, R. Calvo, S. Patnaik, X. Hu, Q. Gao, M. Yang, M. Lawas, M. Delling, J. Marugan, M. Ferrer, H. Xu, MCOLN1 is a ROS sensor in lysosomes that regulates autophagy, *Nat. Commun.* 7 (2016) 12109.
- [25] P. Atakpa, N.B. Thillaiappan, S. Mataragka, D.L. Prole, C.W. Taylor, IP_3 receptors preferentially associate with ER-lysosome contact sites and selectively deliver Ca^{2+} to lysosomes, *Cell Rep.* 25 (2018) 3180–3193, e3187.
- [26] T.W. Chen, T.J. Wardill, Y. Sun, S.R. Pulver, S.L. Renninger, A. Baohan, E. R. Schreiter, R.A. Kerr, M.B. Orger, V. Jayaraman, L.L. Looger, K. Svoboda, D. S. Kim, Ultrasensitive fluorescent proteins for imaging neuronal activity, *Nature* 499 (2013) 295–300.
- [27] E. Brailoiu, T. Rahman, D. Churamani, D.L. Prole, G.C. Brailoiu, R. Hooper, C. W. Taylor, S. Patel, An NAADP-gated two-pore channel targeted to the plasma membrane uncouples triggering from amplifying Ca^{2+} signals, *J. Biol. Chem.* 285 (2010) 38511–38516.
- [28] H.H. Jensen, M. Brohus, M. Nyegaard, M.T. Overgaard, Human calmodulin mutations, *Front. Mol. Neurosci.* 11 (2018) 396.
- [29] X. Wang, X. Zhang, X.-p. Dong, M. Samie, X. Li, X. Cheng, A. Goschka, D. Shen, Y. Zhou, J. Harlow, Michael X. Zhu, David E. Clapham, D. Ren, H. Xu, TPC proteins are phosphoinositide-activated sodium-selective ion channels in endosomes and lysosomes, *Cell* 151 (2012) 372–383.
- [30] W.W. Lin, B.C. Chen, Pharmacological comparison of UTP- and thapsigargin-induced arachidonic acid release in mouse RAW 264.7 macrophages, *Br. J. Pharmacol.* 123 (1998) 1173–1181.
- [31] J. de Juan-Sanz, G.T. Holt, E.R. Schreiter, F. de Juan, D.S. Kim, T.A. Ryan, Axonal endoplasmic reticulum Ca^{2+} content controls release probability in CNS nerve terminals, *Neuron* 93 (2017) 867–881, e866.
- [32] M. Naraghi, E. Neher, Linearized buffered Ca^{2+} diffusion in microdomains and its implications for calculation of $[\text{Ca}^{2+}]$ at the mouth of a calcium channel, *J. Neurosci.* 17 (1997) 6961–6973.
- [33] S.M. Simon, R.R. Llinas, Compartmentalization of the submembrane calcium activity during calcium influx and its significance in transmitter release, *Biophys. J.* 48 (1985) 485–498.
- [34] J. She, W. Zeng, J. Guo, Q. Chen, X.C. Bai, Y. Jiang, Structural mechanisms of phospholipid activation of the human TPC2 channel, *Elife* 8 (2019), e45222.
- [35] M. Mirdita, K. Schutze, Y. Moriwaki, L. Heo, S. Ovchinnikov, M. Steinegger, ColabFold: making protein folding accessible to all, *Nat. Methods* 19 (2022) 679–682.
- [36] E. Neher, Usefulness and limitations of linear approximations to the understanding of Ca^{2+} signals, *Cell Calcium* 24 (1998) 345–357.
- [37] S.J. Pitt, T. Funnell, M. Sitsapesan, E. Ventura, K. Rietdorf, M. Ruas, A. Ganesan, R. Gosain, G.C. Churchill, M.X. Zhu, J. Parrington, A. Galione, R. Sitsapesan, TPC2 is a novel NAADP-sensitive Ca^{2+} -release channel, operating as a dual sensor of luminal pH and Ca^{2+} , *J. Biol. Chem.* 285 (2010) 35039–35046.
- [38] B. Fakler, J.P. Adelman, Control of K_{Ca} channels by calcium nano/microdomains, *Neuron* 59 (2008) 873–881.
- [39] A.J. Morgan, L.C. Davis, K.T.Y. Wagner, A.M. Lewis, J. Parrington, G.C. Churchill, A. Galione, Bidirectional Ca^{2+} signaling occurs between the endoplasmic reticulum and acidic organelles, *J. Cell Biol.* 200 (2013) 789–805.
- [40] M. Koivusalo, B.E. Steinberg, D. Mason, S. Grinstein, In situ measurement of the electrical potential across the lysosomal membrane using FRET, *Traffic* 12 (2011) 972–982.
- [41] B.E. Steinberg, K.K. Huynh, A. Brodovitch, S. Jabs, T. Stauber, T.J. Jentsch, S. Grinstein, A cation counterflux supports lysosomal acidification, *J. Cell Biol.* 189 (2010) 1171–1186.
- [42] L.C. Davis, A.J. Morgan, A. Galione, Acidic Ca^{2+} stores and immune-cell function, *Cell Calcium* 101 (2022), 102516.
- [43] P.G. Hogan, The STIM1-ORAI1 microdomain, *Cell Calcium* 58 (2015) 357–367.
- [44] L.H. Tay, L.E. Dick, W. Yang, M. Mank, O. Griesbeck, D.T. Yue, Nanodomain Ca^{2+} of Ca^{2+} channels detected by a tethered genetically encoded Ca^{2+} sensor, *Nat. Commun.* 3 (2012) 778.
- [45] G. Csordas, A.P. Thomas, G. Hajnoczky, Quasi-synaptic calcium signal transmission between endoplasmic reticulum and mitochondria, *EMBO J.* 18 (1999) 96–108.
- [46] R. Rizzuto, M. Brini, M. Murgia, T. Pozzan, Microdomains with high Ca^{2+} close to IP_3 -sensitive channels that are sensed by neighboring mitochondria, *Science* 262 (1993) 744–747.
- [47] H. Qi, L. Li, J. Shuai, Optimal microdomain crosstalk between endoplasmic reticulum and mitochondria for Ca^{2+} oscillations, *Sci. Rep.* 5 (2015) 7984.
- [48] H. Vais, J.K. Foskett, D.O. Mak, Unitary Ca^{2+} current through recombinant type 3 InsP_3 receptor channels under physiological ionic conditions, *J. Gen. Physiol.* 136 (2010) 687–700.
- [49] A. Demuro, A. Penna, O. Safrina, A.V. Yeromin, A. Amcheslavsky, M.D. Cahalan, I. Parker, Subunit stoichiometry of human Orai1 and Orai3 channels in closed and open states, *Proc. Natl. Acad. Sci. U.S.A.* 108 (2011) 17832–17837.
- [50] P.J. Church, E.F. Stanley, Single L -type calcium channel conductance with physiological levels of calcium in chick ciliary ganglion neurons, *J. Physiol. (Lond.)* 496 (Pt 1) (1996) 59–68.
- [51] I. Bezprozvanny, B.E. Ehrlich, Inositol (1,4,5)-trisphosphate (InsP_3)-gated Ca^{2+} channels from cerebellum: conduction properties for divalent cations and regulation by intraluminal calcium, *J. Gen. Physiol.* 104 (1994) 821–856.
- [52] F. Marie-Anais, J. Mazzolini, F. Herit, F. Niedergang, Dynamin-actin cross talk contributes to phagosome formation and closure, *Traffic* 17 (2016) 487–499.
- [53] F. Niedergang, S. Grinstein, How to build a phagosome: new concepts for an old process, *Curr. Opin. Cell Biol.* 50 (2018) 57–63.
- [54] C. Czibener, N.M. Sherer, S.M. Becker, M. Pypaert, E. Hui, E.R. Chapman, W. Mothes, N.W. Andrews, Ca^{2+} and synaptotagmin VII-dependent delivery of lysosomal membrane to nascent phagosomes, *J. Cell Biol.* 174 (2006) 997–1007.
- [55] E. Brailoiu, J.L. Hoard, C.M. Filipeanu, G.C. Brailoiu, S.L. Dun, S. Patel, N.J. Dun, Nicotinic acid adenine dinucleotide phosphate potentiates neurite outgrowth, *J. Biol. Chem.* 280 (2005) 5646–5650.
- [56] P.K. Aley, A.M. Mikolajczyk, B. Munz, G.C. Churchill, A. Galione, F. Berger, Nicotinic acid adenine dinucleotide phosphate regulates skeletal muscle differentiation via action at two-pore channels, *Proc. Natl. Acad. Sci. U.S.A.* 107 (2010) 19927–19932.
- [57] G.C. Brailoiu, B. Gurzu, X. Gao, R. Parkesh, P.K. Aley, D.I. Trifa, A. Galione, N. J. Dun, M. Madesh, S. Patel, G.C. Churchill, E. Brailoiu, Acidic NAADP-sensitive calcium stores in the endothelium: agonist-specific recruitment and role in regulating blood pressure, *J. Biol. Chem.* 285 (2010) 37133–37137.
- [58] C.E. Bastian-Eugenio, A. Bohorquez-Hernandez, J. Pacheco, A. Sampieri, A. Asanov, J.P. Ocelotl-Oviedo, A. Guerrero, A. Darszon, L. Vaca, Heterologous calcium-dependent inactivation of Orai1 by neighboring TRPV1 channels modulates cell migration and wound healing, *Commun. Biol.* 2 (2019) 88.
- [59] P. Kar, C. Nelson, A.B. Parekh, Selective activation of the transcription factor NFAT1 by calcium microdomains near Ca^{2+} release-activated Ca^{2+} (CRAC) channels, *J. Biol. Chem.* 286 (2011) 14795–14803.
- [60] G. Santulli, R. Nakashima, Q. Yuan, A.R. Marks, Intracellular calcium release channels: an update, *J. Physiol. (Lond.)* 595 (2017) 3041–3051.
- [61] M.T. Nelson, H. Cheng, M. Rubart, L.F. Santana, A.D. Bonev, H.J. Knot, W. J. Lederer, Relaxation of arterial smooth muscle by calcium sparks, *Science* 270 (1995) 633–637.
- [62] G. Grynkiewicz, M. Poenie, R.Y. Tsien, A new generation of Ca^{2+} indicators with greatly improved fluorescence properties, *J. Biol. Chem.* 260 (1985) 3440–3450.
- [63] N. Farneli, O.A. Ogunbayo, C. van Breemen, A.M. Evans, Cytoplasmic nanofunctions between lysosomes and sarcoplasmic reticulum are required for specific calcium signaling, *PLoS One* 14 (2019) 93.
- [64] S. Yamaguchi, A. Jha, Q. Li, A.A. Soyombo, G.D. Dickinson, D. Churamani, E. Brailoiu, S. Patel, S. Muallem, Transient receptor potential mucolipin 1 (TRPML1) and two-pore channels are functionally independent organellar ion channels, *J. Biol. Chem.* 286 (2011) 22934–22942.
- [65] C.C. Chen, C. Cang, S. Fenske, E. Butz, Y.K. Chao, M. Biel, D. Ren, C. Wahl-Schott, C. Grimm, Patch-clamp technique to characterize ion channels in enlarged individual endolysosomes, *Nat. Protoc.* 12 (2017) 1639–1658.
- [66] S. Patel, Deviant lysosomal Ca^{2+} signalling in neurodegeneration. An introduction, *Messenger (Los Angel)* 5 (2016) 24–29.
- [67] J. Wu, L. Liu, T. Matsuda, Y. Zhao, A. Rebane, M. Drobizhev, Y.F. Chang, S. Araki, Y. Arai, K. March, T.E. Hughes, K. Sagou, T. Miyata, T. Nagai, W.H. Li, R. E. Campbell, Improved orange and red Ca^{2+} -indicators and photophysical considerations for optogenetic applications, *ACS Chem. Neurosci.* 4 (2013) 963–972.
- [68] J. Wu, D.L. Prole, Y. Shen, Z. Lin, A. Gnanasekaran, Y. Liu, L. Chen, H. Zhou, S. R. Chen, Y.M. Usachev, C.W. Taylor, R.E. Campbell, Red fluorescent genetically encoded Ca^{2+} indicators for use in mitochondria and endoplasmic reticulum, *Biochem. J.* 464 (2014) 13–22.
- [69] J.M. Falcon-Perez, R. Nazarian, C. Sabatti, E.C. Dell'Angelica, Distribution and dynamics of Lamp1-containing endocytic organelles in fibroblasts deficient in BLOC-3, *J. Cell. Sci.* 118 (2005) 5243–5255.

- [70] E.F. Pettersen, T.D. Goddard, C.C. Huang, E.C. Meng, G.S. Couch, T.I. Croll, J. H. Morris, T.E. Ferrin, UCSF ChimeraX: structure visualization for researchers, educators, and developers, *Protein Sci.* 30 (2021) 70–82.
- [71] J. Akerboom, N. Carreras Calderon, L. Tian, S. Wabnig, M. Prigge, J. Tolo, A. Gordus, M.B. Orger, K.E. Severi, J.J. Macklin, R. Patel, S.R. Pulver, T.J. Wardill, E. Fischer, C. Schuler, T.W. Chen, K.S. Sarkisyan, J.S. Marvin, C.I. Bargmann, D. S. Kim, S. Kugler, L. Lagnado, P. Hegemann, A. Gottschalk, E.R. Schreiter, L. L. Looger, Genetically encoded calcium indicators for multi-color neural activity imaging and combination with optogenetics, *Front. Mol. Neurosci.* 6 (2013) 2.
- [72] E. Neher, Vesicle pools and Ca^{2+} microdomains: new tools for understanding their roles in neurotransmitter release, *Neuron* 20 (1998) 389–399.
- [73] H. Kasai, O.H. Petersen, Spatial dynamics of second messengers: IP_3 and cAMP as long-range and associative messengers, *Trends Neurosci.* 17 (1994) 95–101.
- [74] A.J. Morgan, F.M. Platt, E. Lloyd-Evans, A. Galione, Molecular mechanisms of endolysosomal Ca^{2+} signalling in health and disease, *Biochem J.* 439 (2011) 349–374.
- [75] A. Saminathan, J. Devany, A.T. Veetil, B. Suresh, K.S. Pillai, M. Schwake, Y. Krishnan, A DNA-based voltmeter for organelles, *Nat. Nanotechnol.* 16 (2021) 96–103.
- [76] J.G. Park, A.E. Palmer, Measuring the in situ K_d of a genetically encoded Ca^{2+} sensor, *Cold Spring Harb. Protoc.* 2015 (2015) pdb prot076554.
- [77] L. Tian, S.A. Hires, T. Mao, D. Huber, M.E. Chiappe, S.H. Chalasani, L. Petreanu, J. Akerboom, S.A. McKinney, E.R. Schreiter, C.I. Bargmann, V. Jayaraman, K. Svoboda, L.L. Looger, Imaging neural activity in worms, flies and mice with improved GCaMP calcium indicators, *Nat. Methods* 6 (2009) 875–881.
- [78] X.R. Sun, A. Badura, D.A. Pacheco, L.A. Lynch, E.R. Schneider, M.P. Taylor, I. B. Hogue, L.W. Enquist, M. Murthy, S.S. Wang, Fast GCaMPs for improved tracking of neuronal activity, *Nat. Commun.* 4 (2013) 2170.
- [79] Y. Zhao, S. Araki, J. Wu, T. Teramoto, Y.F. Chang, M. Nakano, A.S. Abdelfattah, M. Fujiwara, T. Ishihara, T. Nagai, R.E. Campbell, An expanded palette of genetically encoded Ca^{2+} indicators, *Science* 333 (2011) 1888–1891.